CODEN: LUTMDN/(TMMV-5362)/1-42/2024

Design and Optimization of a Neutron Polariser for ESS Imaging Instrument ODIN

Maharao Siddhay Vilas

2024

LUND UNIVERSITY

LTH

FACULTY OF ENGINEERING

MASTER THESIS

DIVISION OF PRODUCTION AND MATERIALS ENGINEERING

LUND UNIVERSITY

Supervisor: Dr. Alex Backs

Industrial Superviser: Dr. Wai Tung Lee

Examiner: Dr. Filip Lenrick

Author: Maharao Siddhay Vilas

Lund, Sweden, 2024

CODEN: LUTMDN/(TMMV-5362)/1-42/2024

Abstract

Neutrons have a magnetic moment that interacts with magnetic fields. This has been put to use to study magnetic materials. Polarised neutron imaging (PNI) is one such application that allows the observation of, for instance, magnetic domains and domain walls inside a sample. To facilitate a PNI experiment, the neutron beam from a neutron source needs to be polarised – meaning that the magnetic moments of all neutrons are aligned with an applied magnetic field. The device used to achieve this is called a "Polariser". The focus of this thesis is the design of a polariser for the ODIN imaging instrument that is being constructed at the European Spallation Source (ESS). Among the different choices of polarisers, a "v-cavity" geometry will be used, which works on the principle of the polarisation-dependent reflection of neutrons from a surface structure called "polarising supermirror". Here, Monte Carlo ray-tracing simulations are used to study the ODIN beam characteristics and subsequently to evaluate and optimise the polariser design. In addition, the design of a magnetic housing for the polariser is presented. This is needed, because the polarising supermirrors require a magnetic field to function. Using finite element method to compute the magnetic field, a magnetic housing is designed that would satisfy the field strength and field alignment requirements of the polariser.

Keywords: Polarised neutrons, polarised neutron imaging, magnetic domains, neutron imaging instrument, ODIN, European Spallation Source, neutron polariser, polarising supermirror, v-cavity, Monte Carlo method, ray tracing, magnetic field, finite element method.

Table of Contents

1. Introduction

The aim of this study is to carry out an initial design study of a device called "neutron polariser" for use at the future neutron imaging instrument ODIN at the European Spallation Source ("ESS"). The polariser will produce polarised neutrons for polarised neutron imaging experiments on ODIN.

1.1 Polarised neutrons

Neutron has a spin angular momentum of $\hbar/2$ ($\hbar$ = 1.055×10^{-34} J s). This spin angular momentum is associated with a dipole magnetic moment μ_n = -1.910 μ_N (nuclear magneton 1 μ_N = 5.051 $\times10^{-27}$ J/T), which gives rise to interaction between neutron spin and magnetic field. With an applied magnetic field $\vec{B}$ = B $\hat{y}$ defining the quantization axis, as a spin 1/2 particle, there are two quantized spin states σ_y = +1/2 and -1/2. Using the energy equation E = - μ_n σ_y B, the naming convention is to use "spin up" or "spin+" for the high-energy spin state with σ_y = +1/2 and "spin down" or "spin-" for the low-energy spin state with σ_y = -1/2. A beam of neutrons has a mixture of spin-up and spin-down neutrons. The quantity, *polarisation*

$$P = (N^+ - N^-)/(N^+ + N^-) \quad (1)$$

characterizes the beam, where N^+ and N^- are the number of spin-up and spin-down neutrons, respectively. So, if P= +/- 1, the beam is considered to be completely polarised. If P = 0, it is unpolarised. A neutron beam generated by a neutron source such as the up-coming Spallation Neutron Source (ESS) is unpolarised. A "polariser" is often placed in the beam to polarise it to a high degree of polarisation. This thesis reports the design simulation of a polariser. The polariser will be used for polarised neutron imaging application [1] [2] using the future Imaging instrument ODIN at the ESS [3] [4].

1.2 Polarised neutron imaging

The interaction of neutron magnetic moment with magnetic field has been put to use to study the magnetic structure of materials. We illustrate one such application with a polarised imaging example.

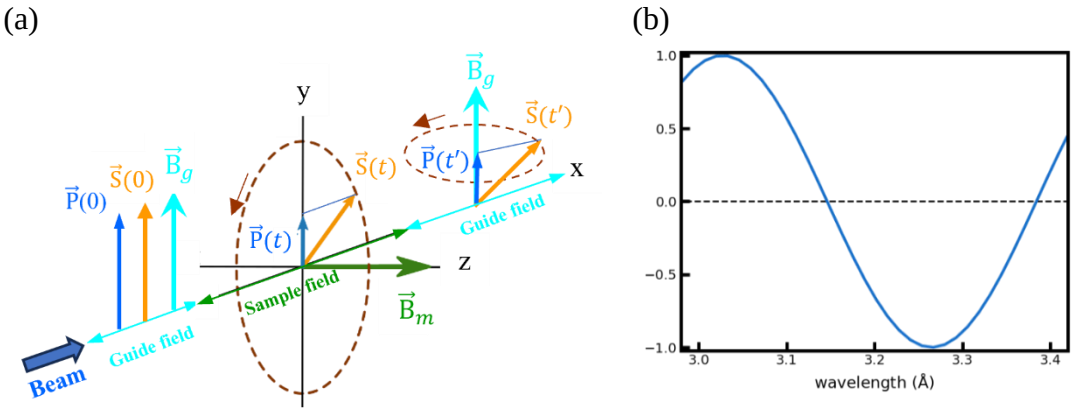

Fig. 1: (a) Schematic diagram of spin rotation in magnetic field, details in text, (b) polarisation as a function of wavelength [5]

In Fig. 1(a), a beam of unpolarised neutrons travelling along direction $\hat{x}$ is first polarised to σ_y = +1/2 state. A guide field $\overrightarrow{B_g} = B_g\,\hat{y}$ is applied along the beam path of the polarised

neutrons. The spin-up neutrons then enter a sample where the guide field has been cancelled out and the magnetic domain in the sample has an internal field $\overrightarrow{B_m} = B_m\,\hat{z}$, which is perpendicular to the guide field. In the quantum mechanical description, the neutron spin state becomes a superposition of +1/2 and -1/2 states, oscillating between the two states in time. This can also be described in an intuitive way in the semi-classical picture, where the neutron beam polarisation is represented by a 3-dimensional vector

$$\vec{S} = S_x\hat{x} + S_y\hat{y} + S_z\hat{z}. \tag{2}$$

The beam polarisation along a direction $\hat{a}$ is given by

$$P = \vec{S}\cdot\hat{a}. \tag{3}$$

The spin-up and spin-down neutron intensities are

$$N^{\pm} = N_0(1 \pm P)/2, \tag{4}$$

Respectively, with the total beam intensity $N_0 = N^+ + N^-$. In this description, the initial beam polarisation vector $\vec{S}$(t=0) = $\hat{y}$ in our example. Inside a magnetic domain, neutron spin *precesses* about the field that is in the $\hat{z}$ direction over time,

$$\vec{S}(t) = sin(\omega_m t)\,\hat{x} + cos(\omega_m t)\,\hat{y}. \tag{5}$$

The *Larmor precession* frequency $\omega_m = \gamma_n B_m$ with γ_n = 1.832×10^8 Hz/T being the neutron gyromagnetic ratio. When neutrons exit the sample and enter the guide field at time T_s, the polarisation vector $\vec{S}(T_s) = sin(\omega_m T_s)\,\hat{x} + cos(\omega_m T_s)\,\hat{y}$. The polarisation component along $\hat{x}$ then precesses about the guide field which is in the $\hat{y}$ direction,

$$\vec{S}(t') = sin(\omega_m T_s)\,cos\big(\omega_g t'\big)\,\hat{x} + cos(\omega_m T_s)\,\hat{y} + sin(\omega_m T_s)\,sin\big(\omega_g t'\big)\,\hat{z}, \tag{6}$$

with frequency $\omega_g = \gamma_n B_g$ and $t' = t - T_s$. Downstream from the sample, an analyser screens the neutrons to allow only neutrons in the +$\hat{y}$ state to reach the detector. Applying equations (3) and (4) to (6), the result is a measurement of the neutron intensity

$$N^{\pm} = N_0\left(1 \pm \vec{S}(t')\cdot\hat{y}\right)/2 = N_0\left(1 \pm cos(\omega_m T_s)\right)/2, \tag{7}$$

Neutrons with different wavelengths spends different among of time T_s in the sample field. The beam polarisation after the sample oscillates as a function of wavelength as seen in fig. 1(b). From there we can learn about the magnetic domains in the sample. For instance, the direction of the magnetization at the domain wall is different from that in the domain, resulting in neutron spin precession different from those passing the middle of the domain. The domains and domain walls therefore have different intensities at the detector.

Such an experiment has been carried out at the BOA imaging instrument at the Paul Scherrer Institute in Switzerland [5]. The setup in the photo in Fig. 2(a) shows the magnetic field environment consisting of two flat solenoids to magnetise the sample, a static magnetic guide field (4.2mT), solid state bender with 4 cm x 4 cm field of view used as an analyser, 2D detector consisting of a LiFl scintillator and a CCD camera. The components such as multi-channel

reflection bender as a polariser, double crystal monochromator used to select a wavelength ($\Delta\lambda/\lambda$=1%), a pinhole and an adiabatic RF spin flipper aren't visible in Fig. 2(a).

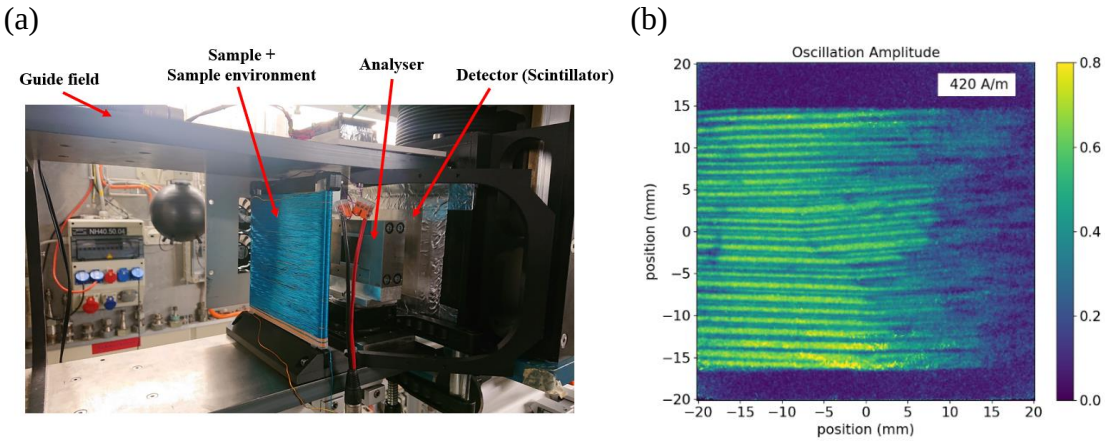

Fig. 2: Polarised neutron imaging experiment on BOA imaging instrument, PSI. (a) Photo of the setup and (b) Image at the detector showing magnetic domains in the sample. (Figures from [5])

The sample used for the experiment is a grain-oriented Si-steel sheet (70 mm x 30 mm x 0.25mm) typically used for application in magnetic cores of transformers. The sample has very large grains (low cm range) and magnetic domains (in the mm range). During the experiment the change of the magnetic domains was investigated upon application of a magnetic field as the key interest was to see macroscopic inhomogeneities in the magnetic response. For the experiment, wavelength scans were performed to analyse the Larmor precession caused by the magnetic domains in the sample which is seen as an oscillation in the measured polarisation as seen in fig. 1(b). An important value obtained from the analysis is the amplitude of this oscillation which can be mainly understood as a measure of the magnetic order. Fig. 2(b) shows the neutron intensity map where magnetic domains can be differentiate from one another. This provides a unique tool to image magnetic domains inside a sample, that would otherwise be difficult if even possible to obtain.

1.3 ODIN imaging instrument at the ESS

Polarised neutron imaging will be implemented on the ODIN imaging instrument that is being built at the ESS in Lund, Sweden. At the ESS, an accelerator will produce proton pulses with 2 GeV proton energy. At a repetition rate of 14 Hz, the proton pulses travelling at 95% speed of light will strike a Tungsten target. The nuclear reaction called "spallation" shatters the tungsten nuclei and generates neutrons [6]. The neutrons, initially travelling at 10% speed of light, are thermalized in moderators consisting of either water, D_2O or liquid hydrogen, to an energy in the meV range, or equivalently from a few Å to 10s of Å in wavelength, that are more suitable for material studies. A portion of the thermal neutrons then enter neutron guides and channeled to the instruments. One of them is the ODIN imaging instrument.

Situated at a target-to-sample distance of 60 m, the ODIN instrument will primarily use a wavelength range from 2.5 Å to 7.5 Å. Refer to fig. 3 above, neutrons from the target ("T") are first moderated, then pass a series of choppers ("Choppers"). The choppers condition and shape the neutron pulse. The neutrons then enter a neutron guide ("Neutron Guide") which is a channel with inner surface coated with neutron reflecting "supermirrors". Based on optical

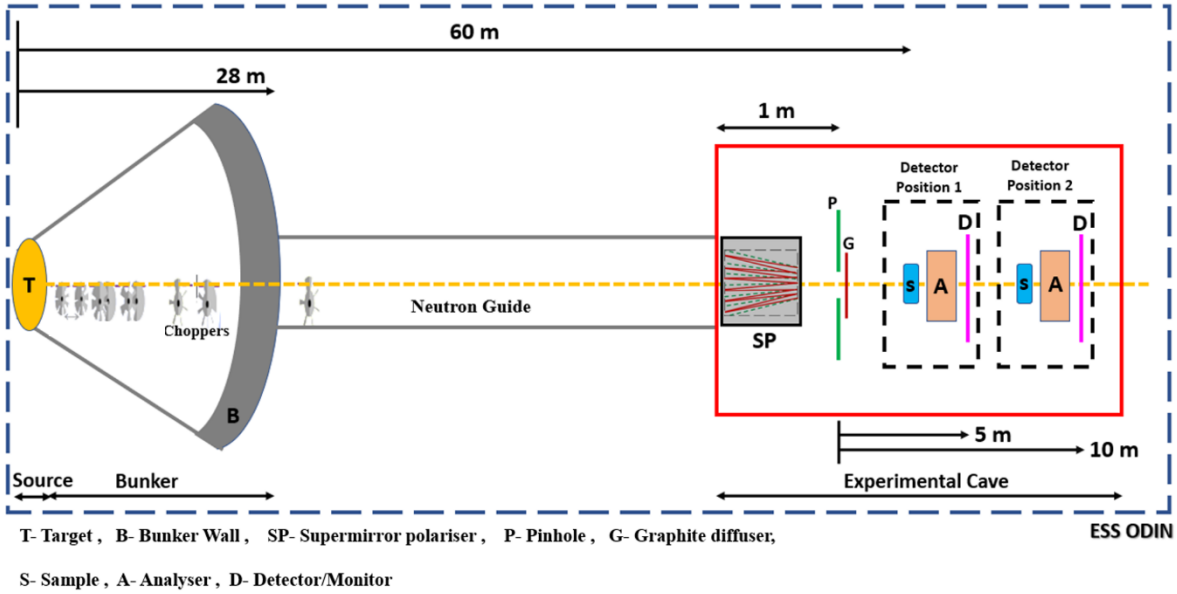

Fig. 3: Schematic diagram of the ODIN instrument

principles, the geometry of the neutron guide is optimized to channel a large flux to the instrument. Upon exiting the neutron guide, the neutron beam focuses at a pinhole ("P") at 1 m from the beam exit. Between the neutron guide exit and the pinhole is a neutron polariser ("SP") which is the focus of this study. After the pinhole, the polarised neutron beam interacts with a sample ("S"). The result of the interaction is measured by first passing the beam through an analyser ("A") to filter the selected polarisation component, then measuring the intensity map at an imaging detector ("D"). There are two available positions of the sample-analyser-detector at 5 m and 10 m detector position, respectively. The choice of the position depends on the resolution needed for the experiment.

2. Neutron Polariser

The device to achieve polarisation is known as "polariser". The main performance parameters of a polariser are the polarisation of the beam that has passed the polariser and the beam transmission through the polariser. The transmission is defined as $T = (N^+ + N^-)/N_0$, where N_0 is the number of neutrons entering the polariser. A majority of polarisers are spin-filters which filter the selected polarisation component either by absorbing neutrons in one of the spin states or by deflecting them away from the beam to other directions.

2.1 Different types of neutron polariser

There are different methods to polarise a neutron beam, and the choice of the best technique depends on the instrument and the experiment to be performed. Polarising the neutron beam can be done by using either polarising crystal, polarising supermirror and polarising filter. Based on this, we have three types of polarisers, namely, ^{3}He Polariser, Heusler crystal polariser and supermirror polariser.

2.1.1 ^{3}He polariser

The schematic in fig. 4(a) shows ^{3}He polariser [7] working on the principle of spin-dependent absorption. The filter cells, as shown in fig. 4(b) are made of quartz or aluminosilicate glass

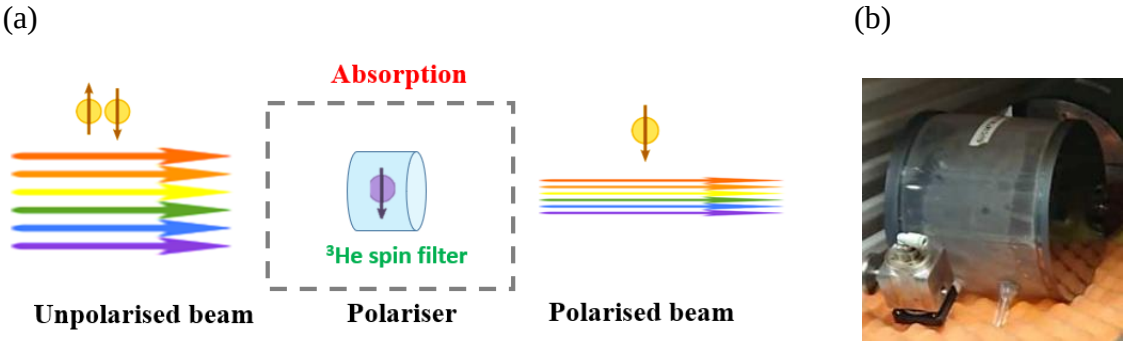

Fig. 4: (a) Illustration of how a ^{3}He polariser works; (b) Photo of a ^{3}He cell. Single-crystal silicon windows are used at the two flat sides of the cell to minimize cell-window interaction with neutrons

and are filled with polarised ^{3}He gas under a certain pressure. There are two most common methods to polarise the ^{3}He gas. In the Metastable-Exchange Optical Pumping (MEOP) method [8], ^{3}He atoms are energized to an excited state by electrical discharge, then optically pumped by a laser, which results in ^{3}He atom being polarised. Hyperfine interaction then polarises the ^{3}He nuclei. In the Spin-Exchange Optical Pumping (SEOP) method [7], the polariser contains a mixture of isotopic helium-3 gas, nitrogen, and alkali vapour. The alkali atoms are optically pumped by a laser. When polarised alkali atoms collide with ^{3}He atoms, ^{3}He nuclei become polarised through a process called spin-exchange interaction.

^{3}He has a large neutron absorption cross-section. This absorption is strongly spin-dependent: large absorption if the ^{3}He and neutron spins are antiparallel, and virtually no absorption if the spins are parallel. Placing a cell of polarised ^{3}He in an incident unpolarised neutron beam selectively removes one of the neutron spin states from the beam while allowing the other spin state to be transmitted. This results in a polarised neutron beam after the polariser. The main advantage of ^{3}He polariser is that the divergence and homogeneity of the neutron beam remains unaffected. On the other hand, ^{3}He polarisation is highly susceptible to magnetic field gradient. It requires special magnetic field elements to produce a homogeneous magnetic field around the ^{3}He filter cells and sufficient distance from magnetic sample and sample magnet. This results in greater sample to detector distance which then reduces the spatial resolution in an imaging experiment. Unless we place ^{3}He polariser directly on the beam – not all instruments can accommodate such a setup, ^{3}He gradually loses polarisation over time. During experiment, periodic replacement of polarised gas by exchanging either the ^{3}He cells or the gas is required. The neutron absorption cross-section of ^{3}He is proportional to the neutron wavelength. The device therefore reaches higher polarisation at longer wavelength, but with a trade-off of a lower transmission.

2.1.2 Heusler alloy polariser

Heusler alloy crystal Cu_2MnAl is a ferromagnet at ambient temperature. The spin-dependent Bragg scattering intensity of a ferromagnetic crystal is proportional to $|F_N \pm F_M|^2$ where F_N and F_M are the nuclear and magnetic structure factor, respectively. The two structure factors sum together for spin-up neutrons and subtract from one another for spin-down neutrons. The structure factor is derived from the Bragg's law and either the nuclear interaction between neutron and nuclei of the material or the magnetic interaction between neutron magnetic moment and the material's magnetization. For the (111) reflection of a magnetically saturated Heusler crystal, $F_N \approx -F_M$. Most reflected neutrons are therefore in the spin-down state. There

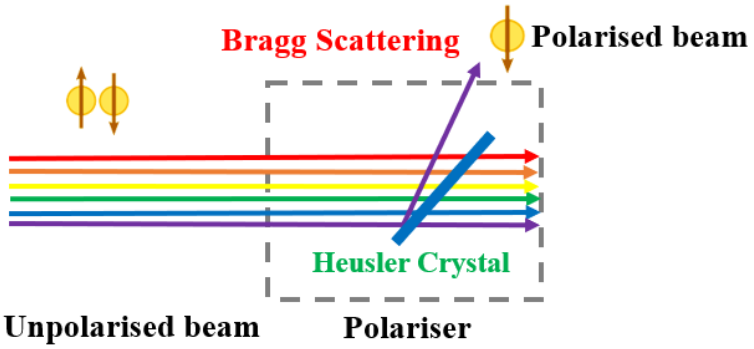

Fig. 5: Illustration of how a Heusler alloy polariser works

is little reflected intensity of spin-up neutrons. At a given angle between the incident beam and the crystal, only neutrons within a narrow wavelength band can satisfy the Bragg scattering condition and be reflected. Heusler alloy polariser [9] is therefore also a monochromator. By adjusting the orientation of the crystal with respect to the incident neutron beam, it is possible to select the desired wavelength of neutrons reflected towards the sample.

2.1.3 Supermirror polariser

Supermirror polariser [10] works on the principle of spin-dependent reflection by surface coatings. There are different geometries for implementing supermirror polarisers. The simplest geometry being one single polarising supermirror. In practice, v-cavity, c-bender, solid state bender and s-bender are some of the commonly found supermirror polarisers [11].

1) Single polarising supermirror

In the illustration in fig. 6, a single polarising supermirror is placed in the path of an unpolarised beam. A combination of Fe and Si coatings on glass substrate is commonly used in polarising supermirrors. At a Fe/Si polarising supermirror, the part of beam with up-spins gets reflected while the rest of the beam with down-spins gets transmitted. Under certain conditions of the wavelength range, divergence, and supermirror reflectivity, both the reflected and transmitted beams can be useful and so the downstream experimental setup can be placed to use either beam as per the experimental requirements.

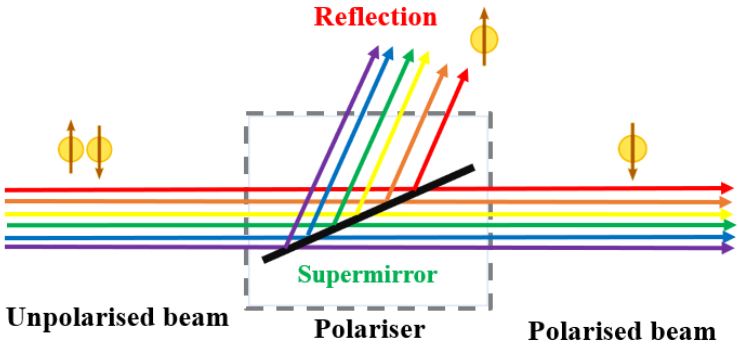

Fig. 6: Illustration of how a supermirror polariser works

The polarising supermirror can be made to cover a broad wavelength band, for instance, from 2.5 Å to 7.5 Å in this study. The polarisation and transmission only change slightly as the wavelength increases. The angle between the incident beam and the supermirror surface however is often just a few degrees. It is often necessary to use multiple channels, each containing a set of supermirrors, to cover the beam cross-section, otherwise it would require

using an impractically long supermirror. As we shall discuss in a subsequent section on the principle of a polarising supermirror, the performance is dependent on the angle between the incident neutron and the supermirror. For a beam with certain divergence, this results in a change in performance across the beam divergence profile.

2) V-cavity

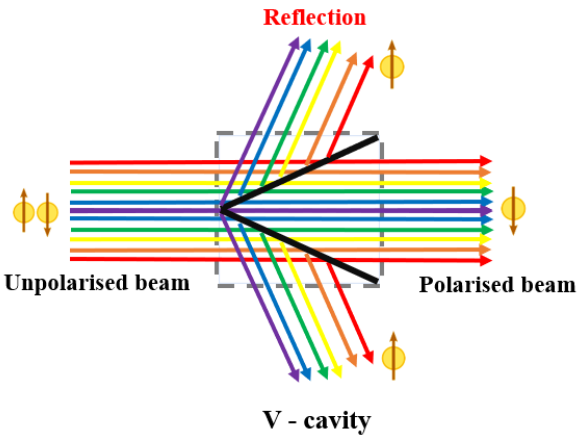

Fig. 7: Illustration of how v-cavity works

A single v-cavity consists of two polarising supermirrors in a "v" shape geometry. It is a transmission polariser. The reflected up-spin neutrons are absorbed by the channel's walls. Compare to a single supermirror, a single v-cavity has half the length. As a v-cavity is a polarising supermirror device, for large beam cross-section, multiple channels of v-cavity can be used to fit a v-cavity within a limited length while covering the beam cross-section. One of the advantages of v-cavity is that, for an incident beam with a certain degree of divergence, a v-cavity eliminates the distortion of the divergence of the transmitted beam towards one side in the case of a single supermirror.

3) C-bender

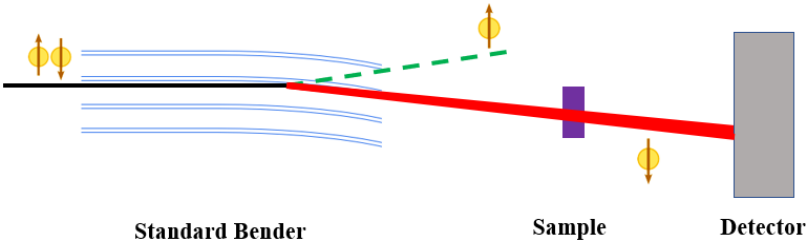

Fig. 8: Illustration of how c-bender works

A c-bender is comprised of bent glass strips covered with a polarising supermirror. As shown in above schematic, neutrons with downward spins are reflected at the surface, while neutrons with upward spins pass through the coating and are captured in a Gd layer beneath the supermirror coating layer. The c-bender changes the direction of the neutron beam. As a polariser, this places restriction on the beamline geometry, but it can also be an advantage for instruments that use a bended beam line geometry to avoid the line of sight to the neutron source, which reduces its fast-neutron background. It also found application as an analyser in scattering instruments: as an analyser for a scattering instrument, the change of beam direction

is not critical. The detectors are placed immediately after the analyser. The angular shift introduced by the c-bender can be corrected. However, c-bender is not suitable as an analyser in polarised imaging applications. Imaging required considerably higher resolution compare to scattering measurements. The c-bender increases the beam divergence through the reflection of the beam on the bent channels, resulting in poor spatial resolution recorded at the detector, smearing the image. The c-bender also introduce inhomogeneity that is difficult to correct as it is difficult to isolate the effect of inhomogeneity from the smearing.

4) Solid state bender

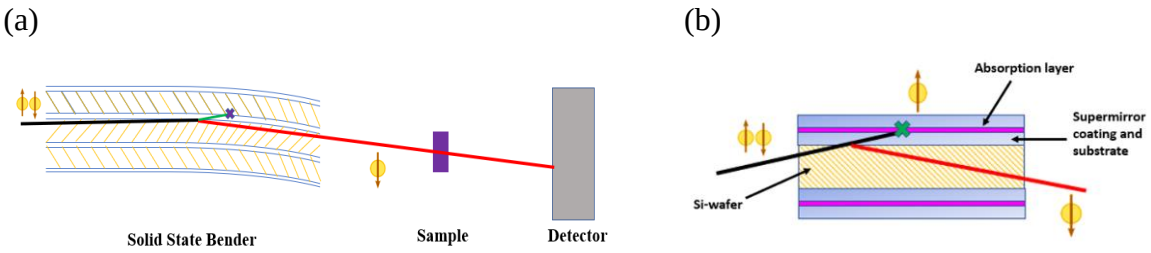

Fig. 9: Illustration of how solid-state bender works. (a) Geometry of the bender and its relation to the subsequent beamline components; (b) Zoom-in view to show the effect of the polarising supermirror coating and the neutron-absorbing Gd coating beneath the supermirror coating

The cross-section of a solid-state bender is drastically decreased by using a set of thin, bent silicon wafers which are coated with a polarising supermirror layer, as shown in fig. 9 above. The neutrons of up spin states travel through the Si, while neutrons with the down spin states are transmitted via the supermirror coating and gets absorbed in a Gd layer beneath the supermirror coating on other side of substrate. The neutron beam entering one of these channels will exit from the same channel on the other end of the bender. These kinds of benders are mostly suited as an analyser, since it can be relatively compact in size which is important as the distance between the sample and detector has to be relatively small for higher spatial resolution. On the other hand, the beam profile becomes inhomogeneous due to differences in the performance between the supermirrors. Careful calibration work needs to be carried out before using the device.

2.1.4 Choice of technology for ODIN polariser: polarising supermirror

The wavelength band on ODIN for polarisation work is 2.5 Å to 7.5 Å. The beam cross section at the exit of the neutron guide is 30 mm width by 45 mm height. As described above, the beam focuses at 1 m from the neutron guide exit to a pinhole, i.e. there cannot be a change in the beam divergence or beam direction by the polariser. These characteristics narrow the choice of polariser technology to between v-cavity and polarised ^{3}He. Comparing the two techniques, the main differences being that the V-cavity has higher transmission at longer wavelengths and polarised ^{3}He leave the homogeneity of the beam unchanged. For a polariser at a distance to the sample, the homogeneity of the beam at the polariser exit does not affect the imaging performance, as the beam divergence smooths out the inhomogeneity over a distance. V-cavity is the technique of choice for the ODIN polariser.

2.2 Principles of polarising supermirror

A v-cavity polariser is an arrangement of polarising supermirrors. The supermirror is based on the principle of neutron reflection from surface structure. In this section, we describe the working principle of polarising supermirrors.

2.2.1 Neutron reflection from a single interface

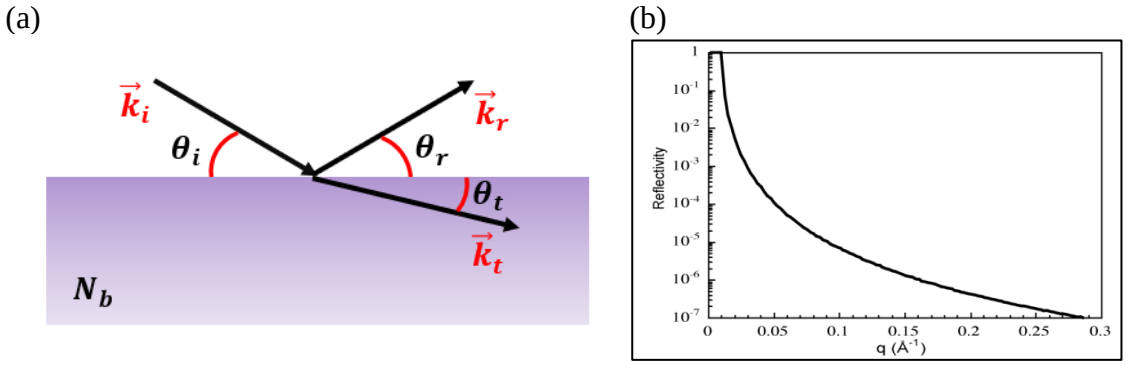

Fig. 9: (a) A neutron beam with wave-vector $\vec{k}_i$ impinges on a surface and split into a reflected beam $\vec{k}_r$ and a transmitted beam $\vec{k}_t$. (b) Reflectivity as a function of moment transfer q. (Figures from [12])

The schematic diagram above shows an incident neutron beam partly reflected at partly transmitted at the interface between the air or vacuum and a thick substrate material with refractive index n. The refractive index depends on the neutron wavelength λ and a parameter called scattering length density N_b,

$$n = 1 - \lambda^2 N_b / 2\pi. \tag{7}$$

The scattering length density depends on a neutron-material interaction parameter called nuclear scattering length b_n and the number density of the nuclei ρ_n and, if there is magnetic interaction, also on magnetic scattering length b_m and the number density of the magnetic moment ρ_m,

$$N_b^{\pm} = \sum_i \rho_{ni}\, b_{ni} \pm \sum_j \rho_{mj}\, b_{mj}, \tag{8}$$

with addition for spin-up neutrons and subtraction for spin-down neutrons, respectively. This is similar to light optics, but the refractive index of neutron for most materials is less than one, i.e. $\theta_t < \theta_i$, and only deviates from one in the order of 10^{-5} – 10^{-6}. So, the reflections only take place at shallow angles. This can be seen through the logarithmic plot of reflectivity (R) against the momentum transfer $q = |\vec{k}_r - \vec{k}_i| = (4\pi/\lambda)\sin(\theta)$ where λ is the neutron wavelength and θ = incident angle (θ_i) = reflection angle (θ_r). It can be noticed that with the increase in q, which can from either an increase in θ or a decrease in λ, the reflectivity decreases rapidly.

2.2.2 Neutron reflection from a single layer of coating on a substrate

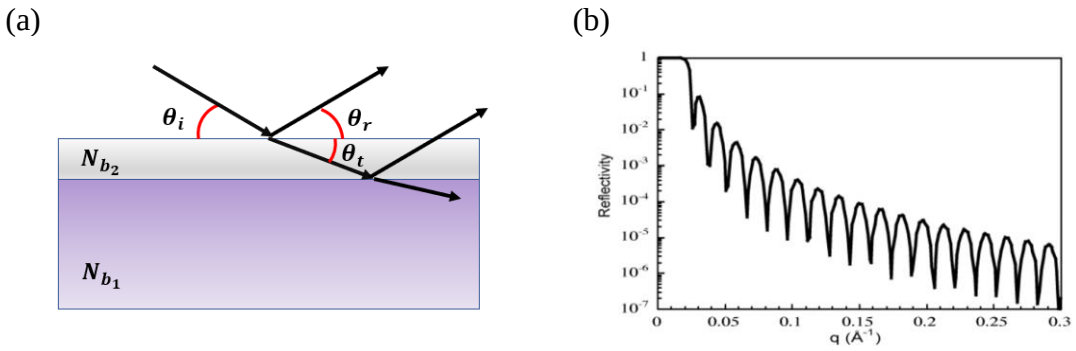

Fig. 10: (a) A neutron beam with wave-vector $\vec{k}_i$ impinges on a surface with a single layer of coating on a substrate. (b) Reflectivity as a function of momentum transfer q. The fringes come from interference between the beams reflected at the two interfaces. (Figures from [12])

The schematic in fig. 10 (a) above shows the reflection from the two interfaces between the three mediums: air or vacuum, a thin layer with refractive index N_{b_2} and a thick substrate with refractive index N_{b_1}. The reflectivity curve is shown in fig. 10 (b). As the incident beam interacts and propagates in the thin layer, it produces multiple reflected and transmitted beams at the two interfaces. The interference between the reflected beams results in the fringes in the reflectivity curve, called Kiessig fringes [13] [14]. The maxima are constructive interference and the minima are destructive interference at intervals of $\Delta q = 2\pi/d$ where d is the layer thickness. The reflectivity is stronger if N_{b_1} and N_{b_2} are more different. On the other hand, if we can tune the material properties so that they have similar scattering length density, the reflection from that interface would disappear and the reflectivity in this case is similar to that of a single interface between air or vacuum and a material with $N_{b_1} \approx N_{b_2}$. For example, for a magnetically saturated iron layer on silicon, we can arrange for the spin-down scattering length density of the Fe layer to match that of silicon whereas the spin-up scattering length density of the Fe layer is more than 6 times that of silicon. So, reflection of spin-down neutrons quickly decreases beyond the total reflection q-value while there is strong reflection of spin-up neutrons from the sample at higher q. This is called contrast-matching and forms the basis of polarising supermirror.

2.2.3 Neutron reflection from a multilayer

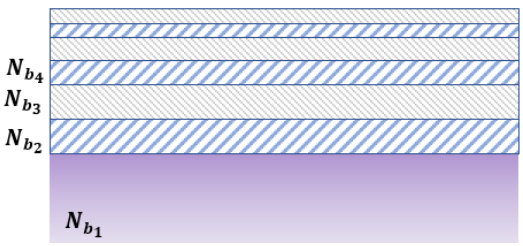

Fig. 11: Schematic diagram of a multilayer

The schematic above shows the layered structure of multiple layers of different materials with respective refractive indices on a thick substrate. The reflectivity curve is a result of reflections and transmissions at each interface and interference between the reflected beams. Two special cases of multilayers are superlattice and supermirror.

a) Superlattice

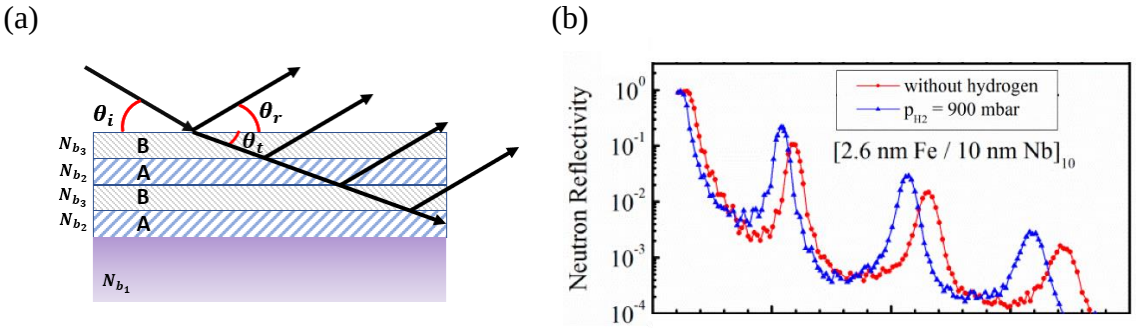

Fig. 12: (a) Schematic diagram of a superlattice (b) Reflectivity of a superlattice [15]

Superlattice is special case where the multilayer consists of repeated arrangement of a set of layers. In most cases, it is a repeat of a bilayer structure, as shown in the schematic diagram in fig. 12(a). The reflectivity of a superlattice is shown in fig. 12(b) [15]. Constructive interference results in sharp maxima occur at intervals of $\Delta q = 2\pi/(d_A + d_B)$ where dA and dB are the thickness of the A and B layers, respectively. The finer pattern overlaying onto the maxima and between the maxima are the Kiessig fringes whose periods are related to each of the A and B layer thickness. With increasing repeats of the bilayers, the intensities of the sharp maxima increase well above the intensity of the Kiessig fringes.

b) Supermirror

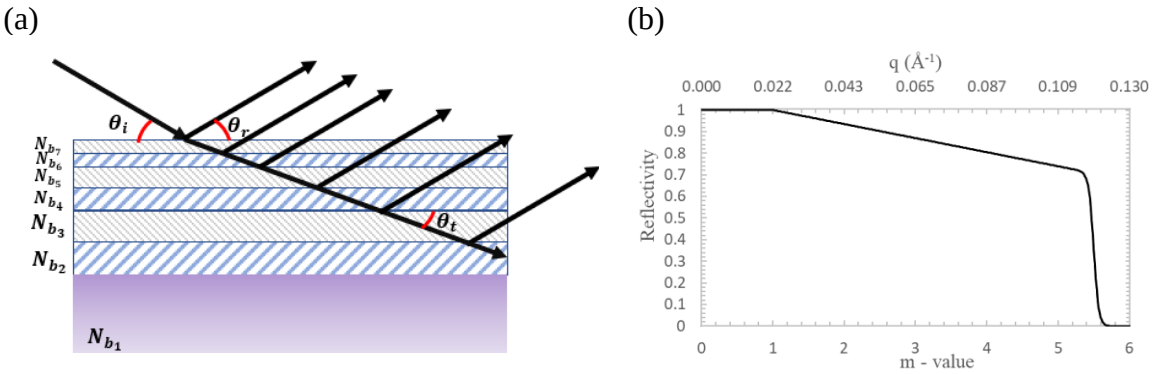

Fig. 13: (a) Schematic diagram of a supermirror (b) Reflectivity of a m=5.5 supermirror

Putting superlattices with different bilayer periods will give rise to reflectivity curve with arrays of maxima with different periods. In the case where the bilayer thickness changes gradually from one set of superlattice to another (fig. 13(a)), the maxima in the reflectivity curve merge together (fig. 13(b)). This is called a supermirror. The reflectivity curve shown in fig. 13(b) comprises of three regions, total reflection up to a critical value of q (as seen 0.022 $Å^{-1}$), slope of the reflectivity and the cut-off region. It can be seen that at higher values of moment transfer

(q), the reflectivity starts dropping linearly with a slope α until it reaches a cut-off value q=m*q_c, where m-value is important parameter used in designing the supermirrors and q_c is moment transfer at critical angle. So, different types of supermirrors can be produced with different critical angles characterized by different m-values.

2.2.4 Polarising supermirror

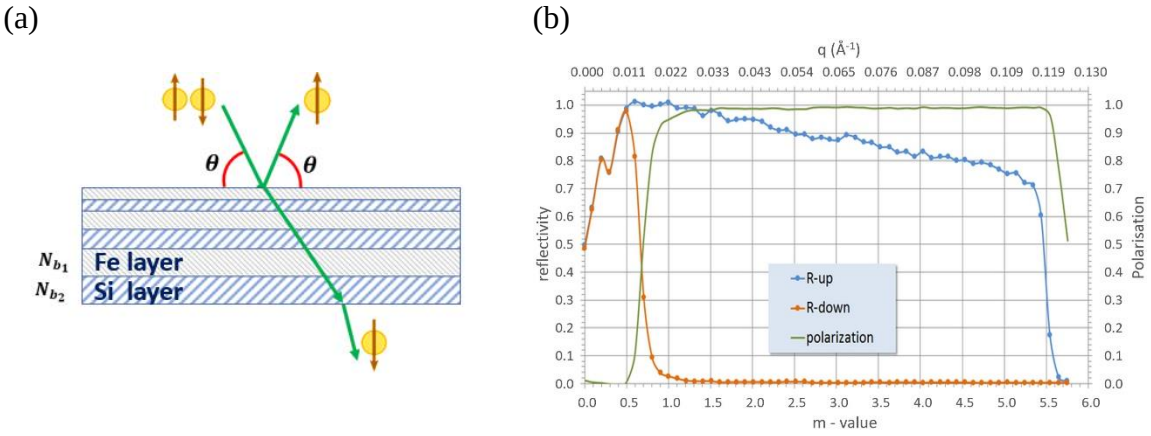

Fig. 14: (a) Schematic diagram of a polarising supermirror (b) Reflectivity of spin-up and spin-down neutrons of a polarising supermirror and the polarisation of the reflected neutron beam [16]

In the case of polarising supermirrors which is the requirement for ODIN polariser design, the materials of the supermirror were chosen such that it reflects only one spin state. The most commonly used materials to achieve this are iron and silicon. As discussed in the section "neutron reflection from a single layer of coating on a substrate", contrast-matching results in most reflected neutrons being spin-up at m > 1. The reflectivity curves of a polarising supermirror [16] is shown in fig. 14 (b) with the up-spin state R-up (blue curve), and the down-spin state R-down (orange curve). The polarisation of the reflected beam is given by (R-up – R-down) / (R-up + R-down) (green curve).

3. Design of ODIN's focusing v-cavity polariser

In the chapters above, we established that the polariser for ODIN will be a v-cavity polariser based on the technology of polarising supermirror and explained how a polarising supermirror function. We now go into the details of the v-cavity design. The goals of the design and optimization of this focused v-cavity design are as follows:

1) to obtain beam polarisation larger than 95% between 2.5 Å to 7.5 Å,
2) to keep the beam transmission as high as possible,
3) to preserve the beam homogeneity,
4) to match the desired field of view (beam cross-section).

3.1 Key considerations of the supermirror layout

There are three key considerations that affects the layout of the supermirrors in the cavity: focusing beam geometry of ODIN, the effect of channelling when using double-side coated polarising supermirror and the finite width of supermirror substrate.

3.1.1 Focusing beam geometry of ODIN

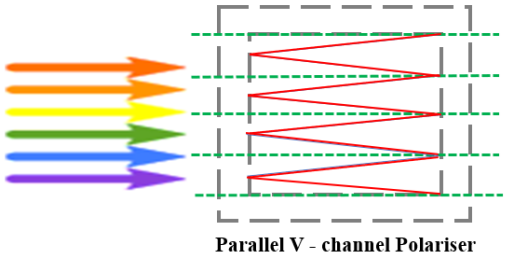

Fig. 15: Parallel V-cavity arrangement

Fig. 15 shows the schematic of a polariser consisting of parallel v-cavities. The walls of all the channels (shown in green) are coated with gadolinium which is a neutron absorbing material. Polarising supermirrors (shown in red) are placed in a v-configuration in every channel. These polarising supermirrors are made of glass substrate coated with alternating Fe and Si layers. In several instruments, the polariser is placed in the part of the neutron guide that has parallel neutron beam. So, we implement this parallel v-cavity arrangement in those instruments.

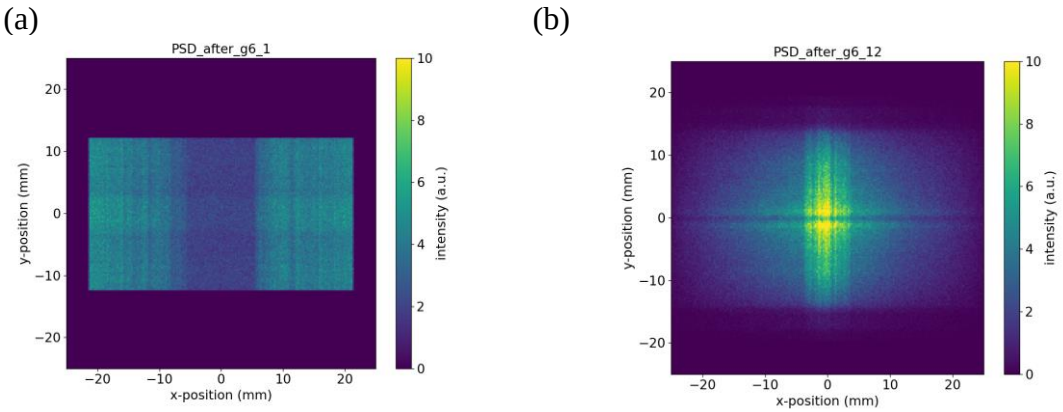

Fig. 16: Beam cross-sections at (a) Detector position 0 cm, (b) Detector position 90 cm

But in the case of ODIN imaging instrument, the main constraint is that the polariser has to be placed at a position, where the beam is focusing. For a focusing beam, the incidence angles of neutrons to the supermirrors in a parallel v-cavity polariser can be larger than what such a setup can accommodate, so we need to modify the geometry of the v-cavity polariser to achieve better performance. Fig. 16 (a) shows the simulated ODIN beam cross-section at the exit of neutron guide system which is 5 mm upstream from the entrance of the v-cavity polariser. It can be observed that as the beam approaches the end of 1 m distance i.e., near the pinhole, the beam is much more focused as shown in fig. 16 (b). Details of the simulation will be given in “Chapter 4” below.

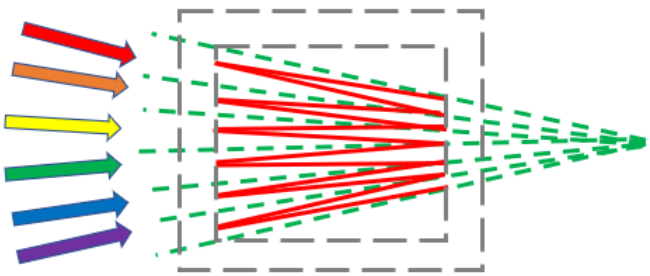

Fig. 17: Focusing v-cavity polariser

Given that the reflection of neutrons is very sensitive to the incident angle and energy of the neutron, the supermirrors need to be precisely oriented and positioned to match the neutron beam's wavelength range, angles, angular divergence, and position. For ODIN, this means matching the focusing geometry of the beam over a wavelength range of 2.5 Å to 7.5 Å. So, we implement new v-cavity arrangement for focusing beam, as shown in fig. 17.

3.1.2 Supermirror arrangement to avoid channelling effect

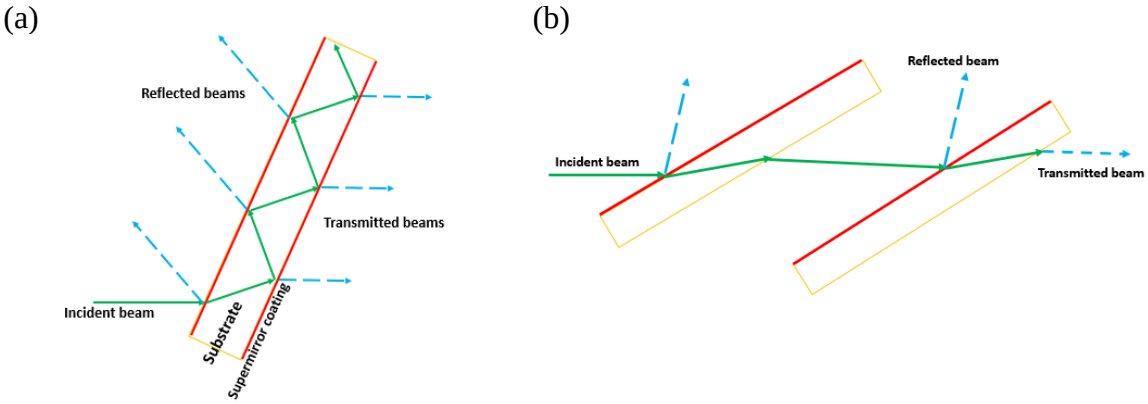

Fig. 18: (a) Channelling effect (b) Avoiding the channelling effect

To achieve better performance, it is often necessary to use more than one polarising supermirror. This can be done by having two polarisers in series but that requires a large space. Alternatively, two polarising supermirrors placed in series in a double v-cavity geometry can be used in a single device. In a number of polarisers, polarising supermirror coatings were applied to both sides of a substrate to further reduce the device length. This however gave rise to a channelling effect that lowered the performance of the supermirror.

The schematics in fig. 18 show two ways of arranging the polarising supermirrors. These mirrors have certain thickness and coating on the substrate, as shown by the red lines. Figure 18 (a) shows the channelling effect in a double-side coated polarising supermirror. Due to both surfaces of the supermirrors having high reflectivity for the unwanted spin state, these neutrons that are reflected from the second supermirror coating bounce back and forth inside. At each reflection, these neutrons have a chance of transmitting through one of the two surfaces. This ultimately lowers the polarisation of the transmitted beam and therefore the performance of the polariser. Thus, to avoid the channelling effect we place two single side coated mirrors a small (~mm) distance apart, as seen in fig. 18 (b). This reduces the channelling effect and improves the polariser performance. This input is relevant while designing the focusing v-cavity for ODIN supermirror polariser.

3.1.3 Finite width of supermirror substrate

With the shallow neutron incident angle required for supermirror, the v-cavity channel is quite narrow in width, usually between 5 to 10 mm. A typical supermirror substrate is 0.5 mm thick. This thickness is sizeable compare to the channel width. Up to 10% neutrons can go through the substrate edge without intersecting the supermirror coating, which will significantly degrade the polariser performance. To ensure neutrons will intersect the supermirror coating, the two supermirrors forming each "v" are offset and positioned to shadow one another.

3.2 Parametrisation of v-cavity

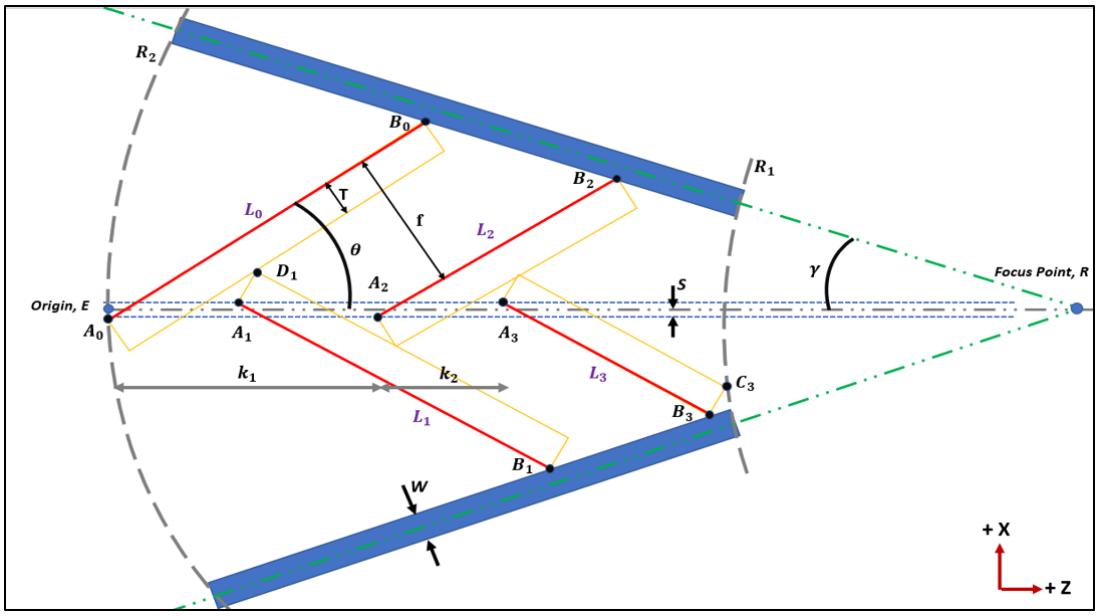

Fig. 19: Schematic of the single channel of the focused v-cavity

Figure 19 shows the design sketch of a single channel in the focused v-cavity for ODIN, using the three key considerations discussed before. It can be seen that there are several supermirrors with certain thickness placed along the z-axis, origin E, focus point R, divider or channel walls, shown in blue. To achieve the above-mentioned goals, it is necessary to understand and calculate parameters such as the separation along the z-axis between the two mirror positions (k_1 and k_2), length of the mirrors (L_i) and half of the opening angle of channel (γ).
For this, we first begin with understanding all the defined or input parameters, as follows,

- R_2 = Focus radius of the channel (it is basically the distance between the entrance of the cavity and the focus point)
- $R_2 - R_1$ = Radial length (it is the length of the device)
- θ = Inclination angle of supermirror (this parameter is based on shortest wavelength, m-value and critical angle of Ni-coating for supermirrors)
- T = Thickness of supermirror
- W = Thickness of dividers
- f = Distance between two supermirrors
- S = Overlap of the supermirrors (this overlap is provided to avoid the case of neutrons passing through the cavity without interacting with the supermirrors)

To finalise the geometry, we need to first take care of certain constraints, such as,

1) The mirrors need to be placed as closely as possible which is constrained by them touching each other at the corner D_1 and then k_2 can be found from the obtained equation.
2) A second constraint for the mirror placement is the minimum distance between parallel mirrors, *f*. From this we obtain a second separation along the z-axis, k_1 , for mirrors 0 and 2 as well as mirrors 1 and 3.

After obtaining the values for k_1 and k_2, we have to finalize which constraint is stronger and that which value needs to be used. For that, we already know that the z-positions of mirrors 0 and 1 are always at 0 and k_2, respectively. So, for mirror 2 we now have to check if 2* k_2 or

k_1 has the maximum value, and that will be used for the placement of the mirrors by also fulfilling both constraints mentioned above. Mirror 3 is then placed at k_2 behind mirror 2.

3) Now we have the mirror positions, but this last mirror with length L_3 should not go outside the device i.e., R_1, which implies that the point C_3 should be touching R_1.
4) Once the above-mentioned constraints are resolved, it can be understood that point B_3 is touching the divider. So, we need to solve for this constraint and through this it's easier approach to find the expression for γ.

Since we will derive the expression for γ, it is now possible to calculate lengths of all the supermirrors.

Other than these parameters, one more important parameter is Mirror adjust angle (θ_{adjust}), which can be given by the equation, $\theta = \theta_{wavelength} - \theta_{adjust}$, where $\theta_{wavelength}$ is an angle necessary for reflection of shortest wavelength and θ_{adjust} is an adjustment angle to account for beam divergence. This $\theta_{wavelength}$ is given by, $\theta_{wavelength} = (Q_m * \lambda)/4\pi$, where $Q_m = m * Q_{c,Nickel}$ (m = m-value for mirror to be designed and $Q_{c,Nickel} = 0.0217 Å^{-1}$, standard base value used while designing the mirrors).

The derivations of the formula for the focused v-cavity geometry is detailed in the Appendix section. The following table summarises the parameters discussed above.

Parameters	Notation	Values
Focus radius of the channel	R_2	≈ 1 m
Radial length of the device	$R_2 - R_1$	0.5 - 0.9 m
Inclination angle of supermirrors	θ	≈ 1°
Thickness of supermirrors	T	0.5 mm
Thickness of dividers	W	0.3 mm
Distance between two supermirrors	f	2 mm
Overlap of the supermirrors	S	< 0.5 mm
Mirror separation along z-axis	k_1	≈ 0.3 m
Mirror separation along z-axis	k_2	≈ 0.15 m
Length of supermirrors	L_i	≈ 0.2 m
Half of the opening angle of channel	γ	≈ 1°

Table 1: Parameters for v-cavity geometry

4. Performance evaluation and optimisation

4.1 McStas, Monte Carlo ray-tracing simulation for neutron instruments

Monte Carlo ray-tracing simulation has been used in capturing the physics of neutron beam. Monte Carlo method is often implemented using computer simulations, and can provide approximate solutions to problems that are otherwise too complex to analyse analytically. It is a sampling method to sample the parameters that characterise neutrons: position, velocity and polarisation vector, at a given time with a corresponding intensity. Ray tracing involves tracking the paths and parametric changes of individual collection of neutrons as they move through the components of a neutron instrument. To understand the relevant polariser performance

parameters such as beam polarisation, transmission, cross-sectional intensity profiles, etc., the McStas simulation software package [17] [18] has been used.

McStas is a software package for simulation of neutron instruments. In McStas, we define the components such as source, neutron guides, monitors, etc. with their respective properties required for the desired instrument setup. Below we provide further details of the entire process:

1) **Source** – The simulation starts will the source component which uses Monte Carlo method to randomly sample the initial neutron parameters: position, velocity, and polarisation vector. The neutron beam intensity associated with each sampling is determined by the physics of the neutron source. Monte Carlo simulation uses repeated sampling to cover the distribution of neutron parameters that characterise the source. The accuracy of the simulation improves with the increase in number of samplings.
2) **Ray propagation –** Ray tracing simulation of neutrons refers to a computationally simulates the behaviour of neutrons as they travel through and interact with various components. After a Monte Carlo sampling chooses one point randomly in the source, the ray propagation begins. In this process, the neutron parameters are passed sequentially to neutron optical components and if needed, also a sample component. In each component, the path of neutron is tracked as it moves through space. Factors such as gravity and magnetic field would be taken into account if the effect on the neutron trajectory or neutron parameters is significant. In our case, gravity has negligible effect so it is not taken into account and magnetic field is implemented implicitly by keeping the polarisation vector unchanged when neutron travels through space. When the neutron trajectory intersects the constituent of a component, such as impinging on the surface of a polarising supermirror, the neutron parameters are changed according to the physics of the interaction, which often changes the neutron trajectory. In the case of the supermirror, the neutron may be reflected from the surface or it may be transmitted and refracted through the surface. The polarising supermirror also changes the polarisation vector of the reflected or transmitted beam. The choice of reflection or transmission uses again Monte Carlo method with the probability of reflection equal to the reflectivity of the supermirror for the corresponding neutron polarisation state.
3) **Monitors –** A monitor or detector component carries out statistical measurements of the neuron parameters and output the relevant information. Various monitors can be used such as intensity cross-sectional profile monitor, polarisation versus wavelength monitor, Time of Flight (TOF) monitor, etc.

4.2 Simulation setup

The setup of components in the simulation match the layout of ODIN described in “Chapter 1, section 3” with modifications to first study the beam focusing in the v-cavity location and then optimise the v-cavity parameters to reach the targeted performance. The v-cavity performance is not dependent on how the choppers shape the time-of-flight profile so all choppers are stopped in the open-position in the simulation.

4.2.1 Setup to study beam focusing

There is a 1-m space between the neutron guide exit and the pinhole. This is the location for the polariser. In order to study the beam focusing in this region, instead of a v-cavity polariser component, position sensitive detector components are placed at 10 cm intervals up to 70 cm from the neutron guide exit, then at 5 cm intervals up to the pinhole (fig. 20). The PSD

component output the cross-sectional beam profile of intensity, polarisation or other parameters of choice.

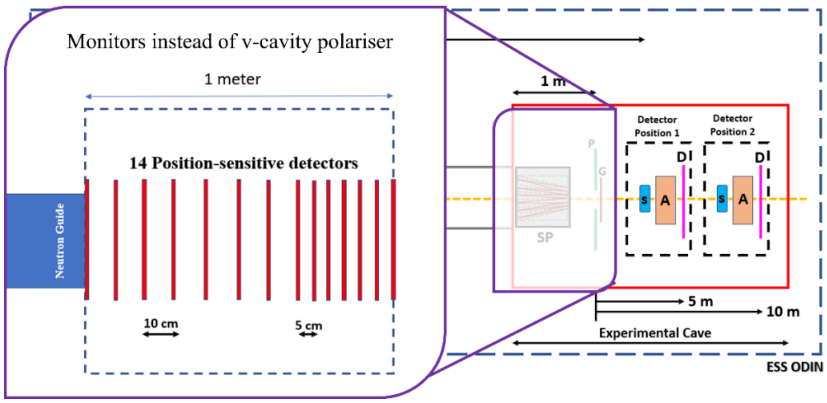

Fig. 20: Implementing ODIN with NO v-cavity for understanding the beam profile

4.2.2 Setup to optimise v-cavity parameters

The schematic in fig. 21 shows the overview of the ODIN instrument setup with the source, neutron guides, polariser v-cavity, pinhole and detectors. Detectors are placed at 4 locations: just before the polariser, just before the pinhole, and at 5 m and 10 m downstream from the pinhole, respectively. At each location, there is a group of 4 detectors: intensity PSD, polarisation PSD, spectrum detector, and polarisation versus wavelength detector.

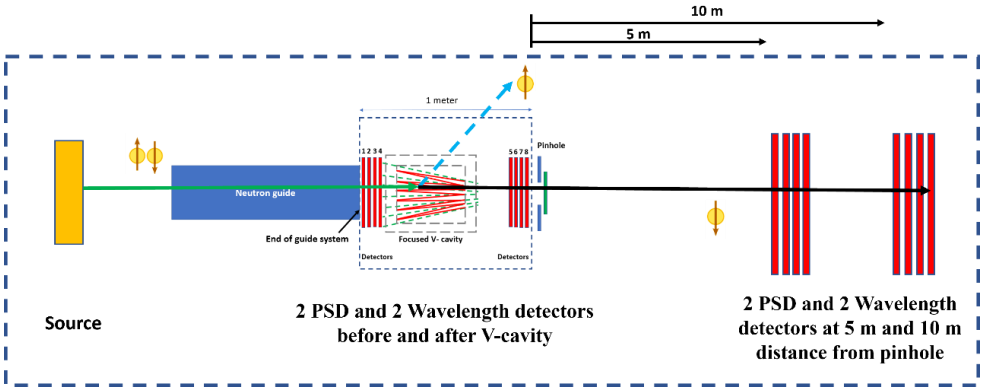

Fig. 21: Implementing Focused V-cavity in ODIN

4.3 Simulation results

4.3.1 Beam focusing

<table>
<tr><td>(a) 0 cm
 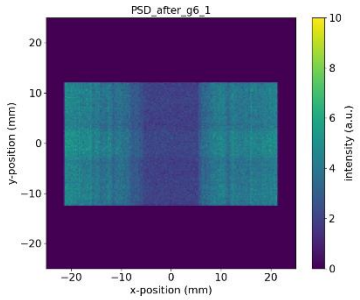
</td><td>(b) 10 cm
 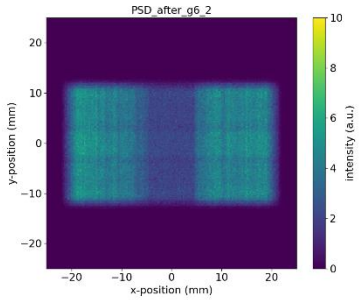
</td><td>(c) 20 cm
 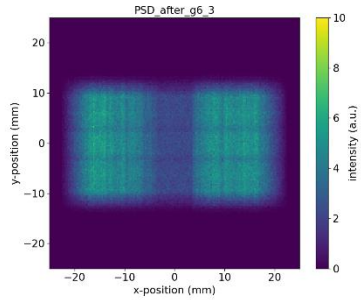
</td></tr>
<tr><td>(d) 30 cm
 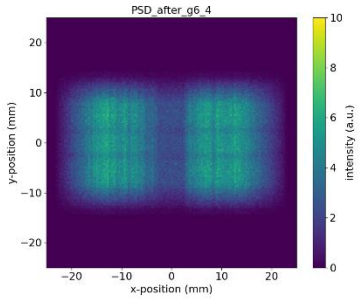
</td><td>(e) 40 cm
 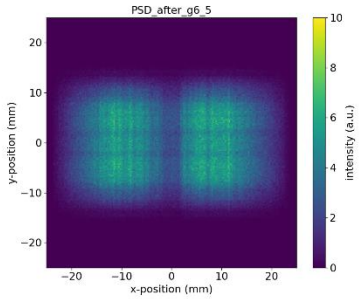
</td><td>(f) 50 cm
 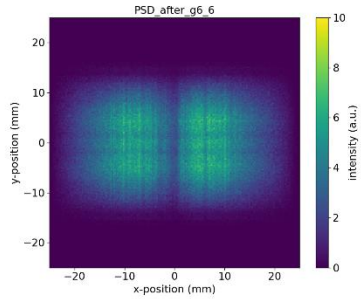
</td></tr>
<tr><td>(g) 60 cm
 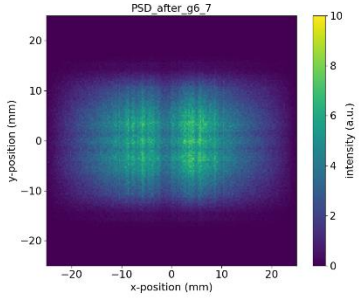
</td><td>(h) 70 cm
 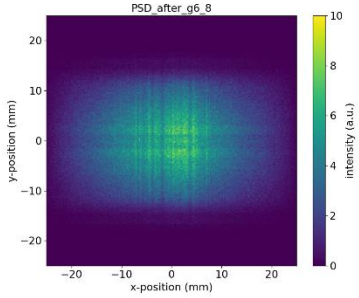
</td><td>(i) 75 cm
 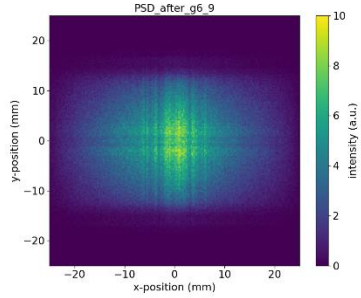
</td></tr>
<tr><td>(j) 80 cm
 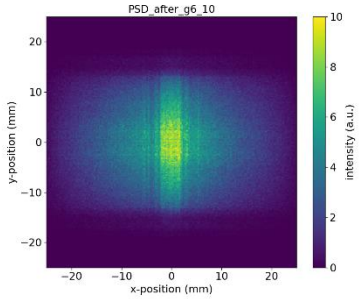
</td><td>(k) 85 cm
 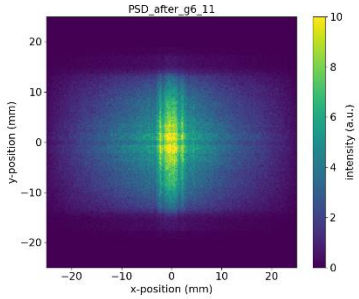
</td><td>(l) 90 cm
 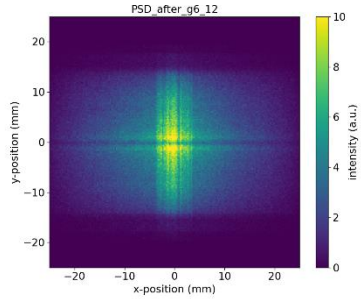
</td></tr>
<tr><td colspan="2">(m) 95 cm</td><td>(n) 100 cm</td></tr>
</table>

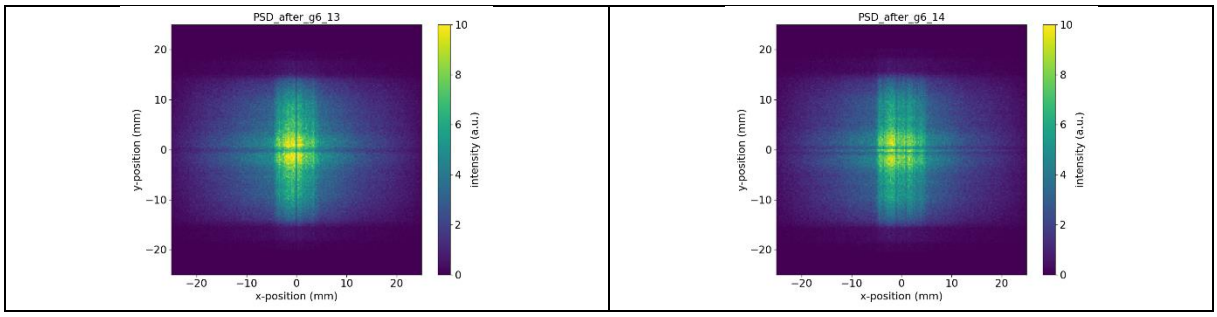

Fig. 22 (a) – (n): Evolution of the beam intensity profile along the 1-m path from the exist of the neutron guide to the pinhole

Fig. 22 (a) to (n) show the cross-sectional beam intensity profile within the 1-m path from the exist of the neutron guide to the pinhole. It can be observed that as the beam approaches towards the end of 1 m distance i.e., near the pinhole, the beam is much more concentrated. The concentration of the neutron flux peaks at about 0.9 m and begins to reduce beyond 0.9 m. It can also be seen that the beam profile primarily consists of two beams converging along z with a much more uniform distribution along y. Matching the polariser geometry to the directions of these two beams is the key for achieving good performance.

The beam intensity distribution is an interplay between the nominal beam direction and beam divergence at different parts of the beam cross-section. While the nominal beam directions converge to a focal point, the beam divergence redistribute the beam intensity in the cross-section along the beam path. This can result in the intensity concentration peaking at a location different from the focal point of the two beams.

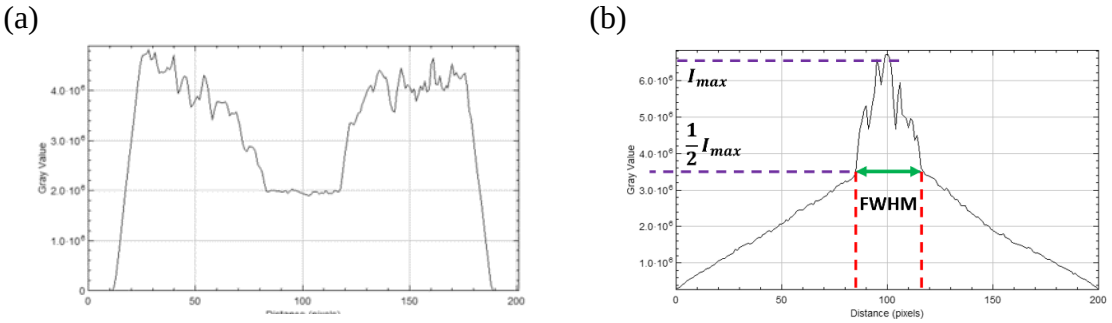

Fig. 23: Vertically integrated Intensity versus horizontal position (a) at 10 cm from guide exit, (b) at 90 cm from guide exit

To identify the focal point, we sum the intensity along y and plot the integrated intensity as a function of position z (fig. 23). Then we fit the profile to obtain the full-width-half-maximum of each profile.

The FWHM as a function of position along the centre beam position is shown in fig. 24. Before the two beam profiles merge, the FWHM decreases linearly. By fitting a line to the data between 0 and 70 cm, the z-intercept at 2.04 m. This is an estimate of the focal point position. From the position at 70 cm from the guide exit to the pinhole at 100 cm, the FWHM of the merged beam profile shows a concentrated beam intensity at the centre. Its value reaches a minimum, indicating the highest beam concentration at about 0.9 m.

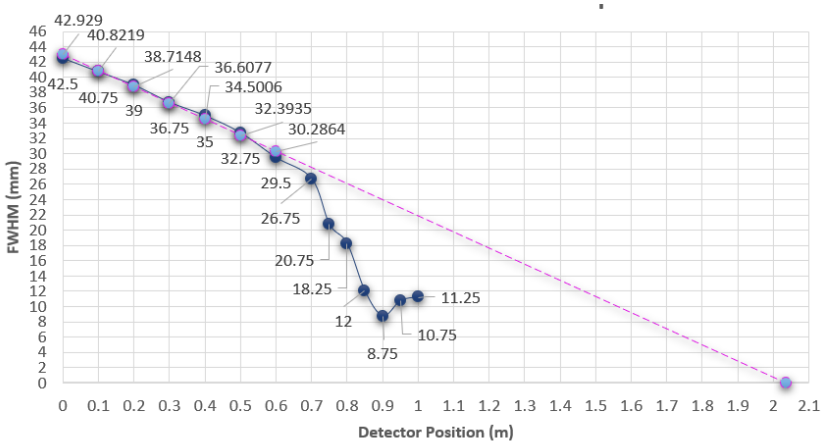

Fig. 24: FWHM as a function of position along the beam direction

The transmission is defined to be the intensity ratio between the intensity recorded by the 3 x 3 cm wavelength monitor (which is the size of pinhole in ODIN) placed at the 1 m distance from the end of neutron guide and the intensity at the neutron guide exit. For reference, the transmission without the polariser is shown in fig. 25. This value is used to normalise all the other beam transmissions data, thus would be termed as Relative beam transmission in further plots.

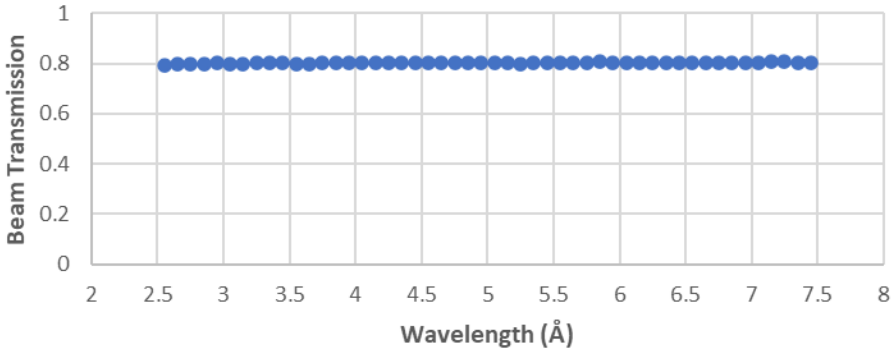

Fig. 25: Transmission as a function of wavelength for the setup without the polariser

4.3.2 V-cavity design optimisation

McStas outputs a plot of the beamline components in the simulation setup. The v-cavity polariser is shown in fig. 26. The plot confirms that the v-cavity setup in the simulation agrees with our design model discussed above. The parameters that remain unchanged for all the simulations are thickness of supermirrors (T = 0.5 mm), thickness of dividers (W = 0.3 mm), distance between two supermirrors (f = 2 mm), overlap of the supermirrors (S < 0.5 mm), m-value (m = 4), ray count = 10000000000 and node count = 30.

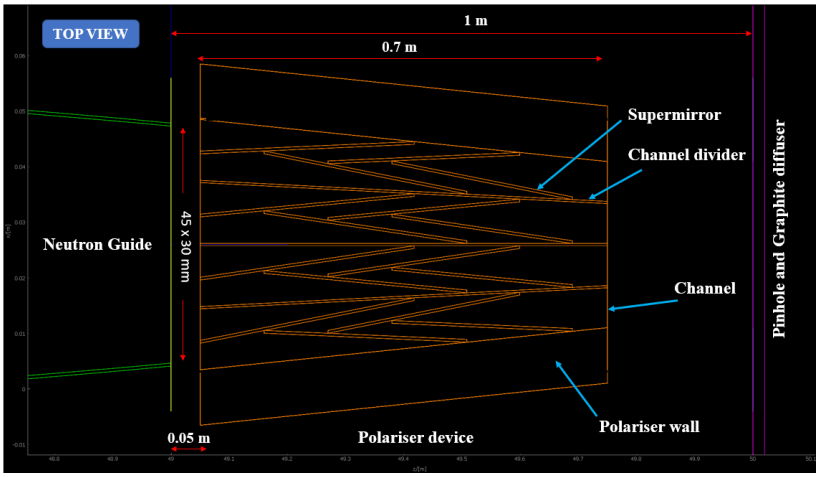

Fig. 26: Plot of v-cavity polariser generated by McStas

First, we check which focal point of the beam profile evaluation shown in Fig. 24 is roughly correct: 0.9 m or 2.04 m. For that we run 10 simulations, with focus radius ranging from 0.7 m to 2.5 m, and device length of 50 cm and m-value = 4 . For each value of focus radius, we find the minimum mirror adjust angle, which change the angle of the supermirrors in the channel to accommodate the beam divergence. A list of the simulations is given in table 2.

Parameters	**Simulation Runs**									
	1	2	3	4	5	6	7	8	9	10
Focus Radius	0.7	0.9	1.1	1.3	1.5	1.7	1.9	2.1	2.3	2.5
Adjust angle	0.29	0.22	0.18	0.15	0.13	0.11	0.10	0.09	0.09	0.08

Table 2: List of parametric values in the simulations

Figure 27 (a) and (b), shows polarization and transmission data over wavelength range. It can be observed that focus radii 0.7 m and 0.9 m are entirely below 95%, focus radii 1.1 m and 1.3 m are worse compared to rest of the lower wavelengths and remaining focus radii listed in table 2 are very similar in trend but comparing them in detail shows which one is the best choice. Supermirrors in general work better for high wavelength which explains why the problem is at low wavelengths. As beam transmission increases with focus radius, it is generally better at low wavelengths.

Looking at the figures 27 (a) and (b), doesn't really help to understand the best choice from the simulation runs, but up on in-depth analysis and comparing the plots for beam polarisation and beam transmission for higher performance over a wavelength range of 2.5 Å to 7.5 Å, it can be realised that for a device length of 50 cm and m-value = 4 , the optimum value produced from the simulations has focus radius of 1.9 m and mirror adjust angle of 0.1°.

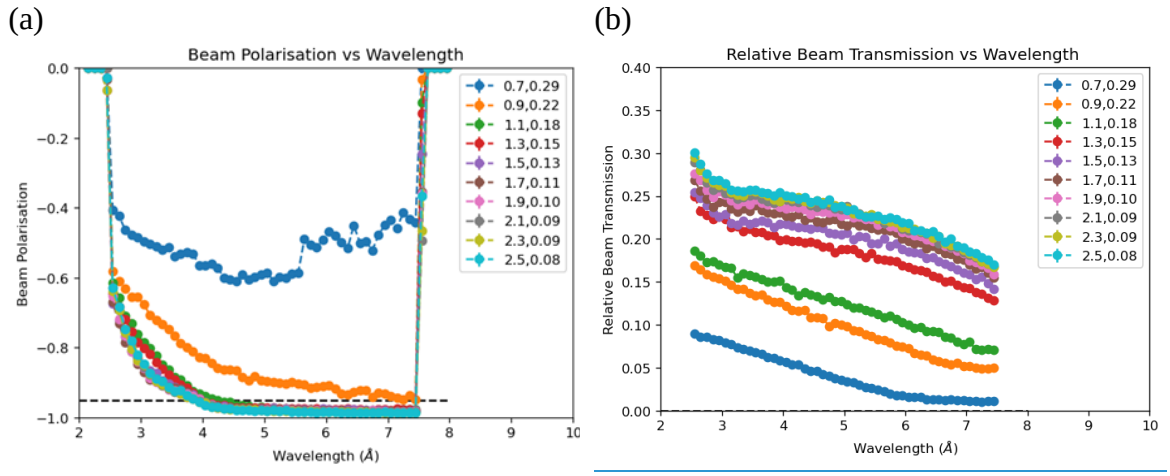

Fig. 27: For v-cavity length = 50 cm, at different focuses and mirror adjust angles (a) beam polarisation vs wavelength (b) relative beam transmission vs wavelength

For the following simulations, the device length was changed to 70 cm, since the simulations for device length 50 cm indicated that a longer cavity would be beneficial as it reduces the number of channels.

The next 3 sets of simulations address the adjust angle for three focus radii values 1.7m, 1.9 m and 2.1 m.

For focus radius = 1.9 m, the mirror adjust angle are increased in steps of 0.01 for every simulation over a wavelength range of 2 – 8 Å. The simulation results are shown in Fig 28 (a) and (b).

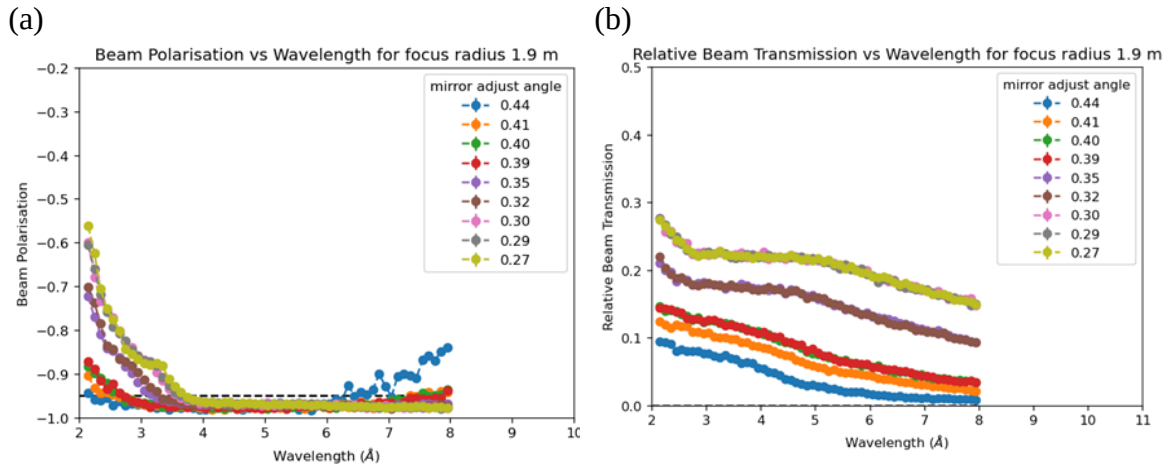

Fig. 28: For focus 1.9 m, at different mirror adjust angles (a) Comparison of beam polarisation vs wavelength (b) Comparison of relative beam transmission vs wavelength

Fig 28 (a), shows similar kind of trend for all adjust angles at lower wavelengths as the polarisation gets better with higher adjust angle because the incident angle gets more shallow. Higher adjust angle means more channels, which means more dividers with absorbing material ultimately leading to lower transmission. Also, better transmission can be seen at lower wavelengths compared to higher wavelengths, as shown in fig. 28 (a) and (b). Up on comparing the beam polarisation and relative beam transmission plots from Fig 28 (a) and (b), it can be understood that, for focus radius 1.9 m with respect to the polarisation, there were 3 plausible

solutions with mirror adjust angles at 0.39°, 0.4° and 0.41°. Upon comparing all the simulation runs, we found that the best solution is with mirror adjust angle = 0.41°, which has polarisation greater than 0.95 (fig. 29 (a)) and maximum transmission (fig. 29 (b)) compared to other two values over a range of 2.5 – 7.5Å wavelength.

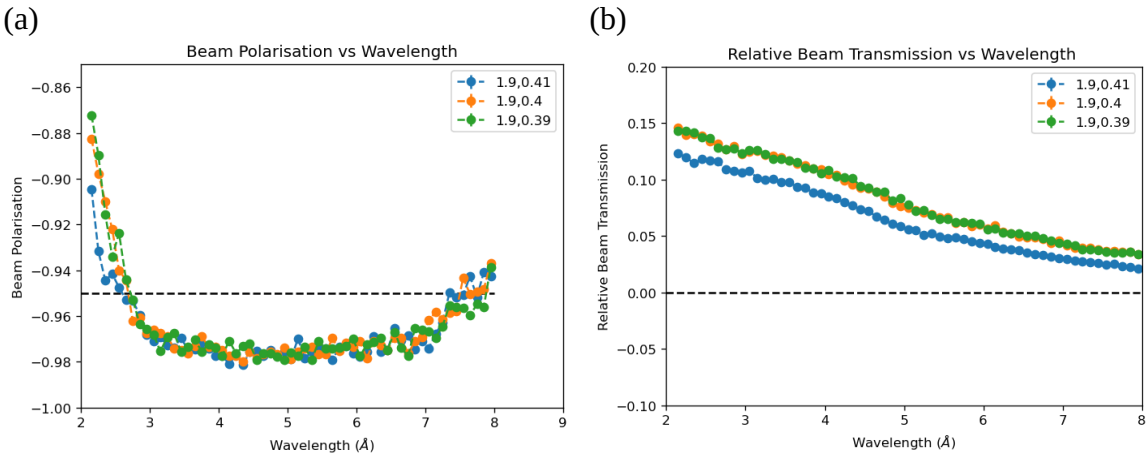

Fig. 29: For focus 1.9 m and three different adjust angles (a) Comparison of beam polarisation vs wavelength (b) Comparison of relative beam transmission vs wavelength.

To check if this focus radius is optimal solution or not, we now decide to check focus radius with one smaller radius value and one larger radius value with regards to 1.9m. So, changing focus radius to 1.7 m and 2.1 m by keeping other parameters unchanged except the mirror adjust angle. For focus radius 1.7 m, we first need to check the minimum mirror adjust angle. The value of this parameter was 0.19°. Then as earlier the mirror adjust angle was increased in steps of 0.01° to find optimal solution over a wavelength range of 2 – 8 Å. The simulation results are shown in Fig.30 (a) and (b).

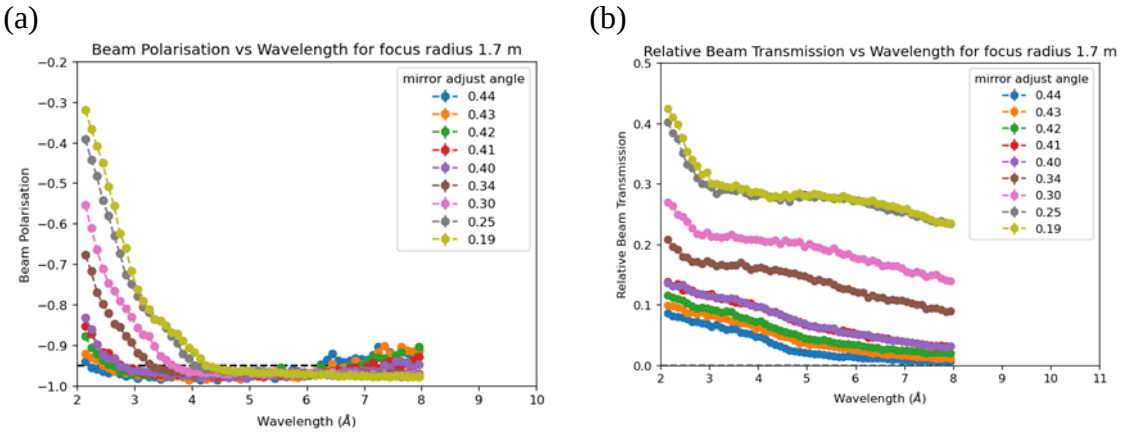

Fig. 30: For focus 1.7 m (a) Comparison of beam polarisation vs wavelength (b) Comparison of relative beam transmission vs wavelength

Comparing the beam polarisation and relative beam transmission plots from Fig. 30 (a) and (b), it can be understood that for focus radius 1.7 m, the trend is similar to plots for 1.9 m (shown in fig 28 (a) and (b)) and so there are 2 optimal solutions with mirror adjust angles as 0.41° and 0.42°. After comparing both the simulations in detail it can be seen that, the best solution is with mirror adjust angle 0.41 degrees as it has polarisation greater than 0.95 (fig. 31 (a)) and maximum transmission (fig. 31 (b)) compared to other value over a range of 2.5 – 7.5Å wavelength.

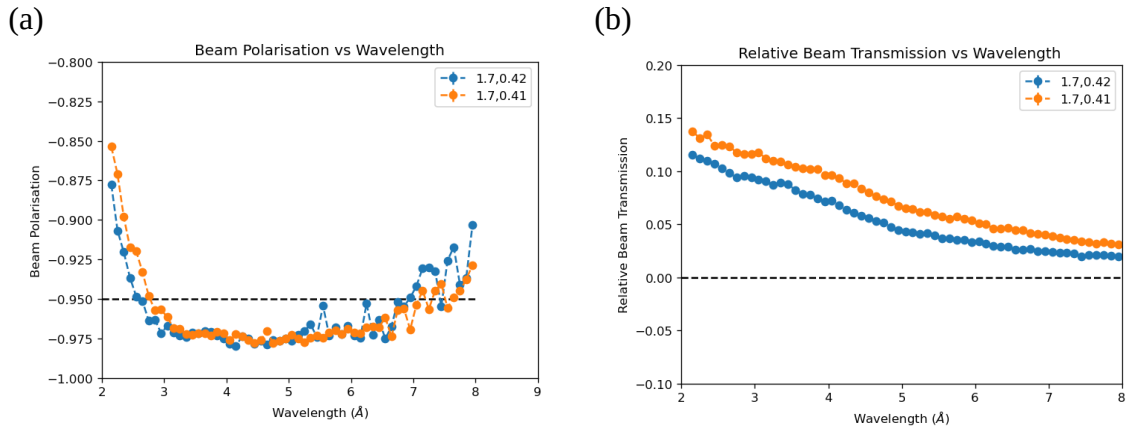

Fig. 31: For focus 1.7 m and two different adjust angles (a) Comparison of beam polarisation vs wavelength (b) Comparison of relative beam transmission vs wavelength

Similarly, for focus radius 2.1 m, the trend shown in fig. 32 (a) and (b) is similar to 1.7 m and 1.9 m plots and the minimum mirror adjust angle determined was 0.16°.

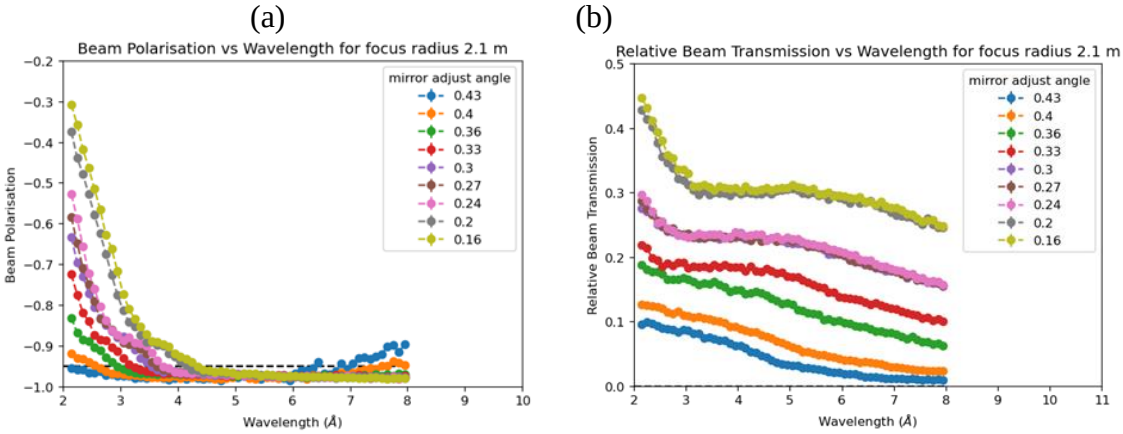

Fig. 32: For focus 2.1 m, (a) Comparison of beam polarisation vs wavelength (b) Comparison of relative beam transmission vs wavelength

Upon running multiple simulations, we found 2 optimal solutions with mirror adjust angles at 0.4° and 0.41°. Upon comparing the two, the best solution has mirror adjust angle 0.4° and has polarisation > 95% (fig. 33 (a)) and higher transmission than other configurations (fig. 33 (b)).

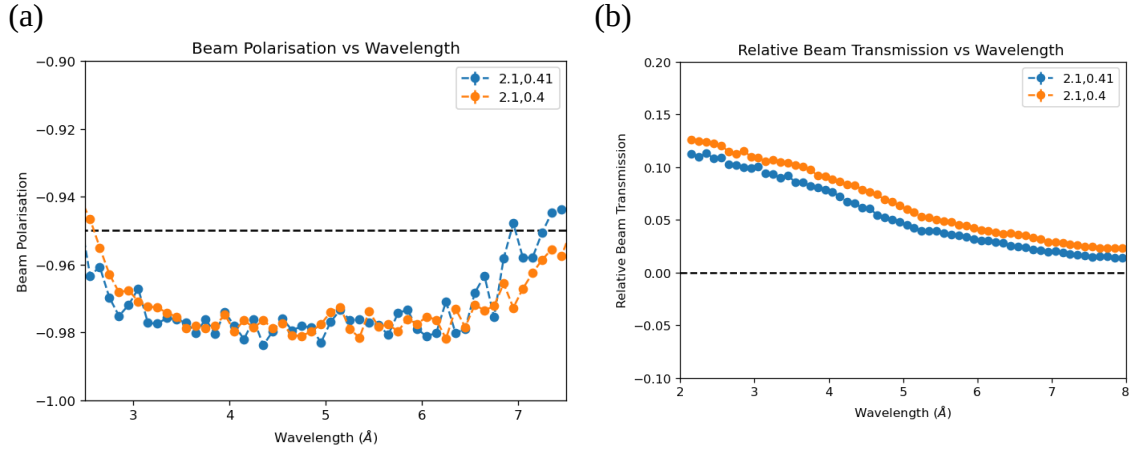

Fig. 33: For focus 2.1 m and two different adjust angles (a) Comparison of beam polarisation vs wavelength (b) Comparison of relative beam transmission vs wavelength

Now, we have three solutions, one for focus radius 1.7 m, another for 1.9 m and the last one for 2.1 m with its respective mirror adjust angles. So, we need to compare these three, to obtain the most efficient value amongst these three best solutions. For that, we run the simulations, and plot the graphs for beam polarisation (fig. 34(a)) and beam transmission (fig. 34 (b)). Upon comparing these it can be understood that the best performance has a focus radius = 2.1 m and mirror adjust angle = 0.4°.

(a) (b)

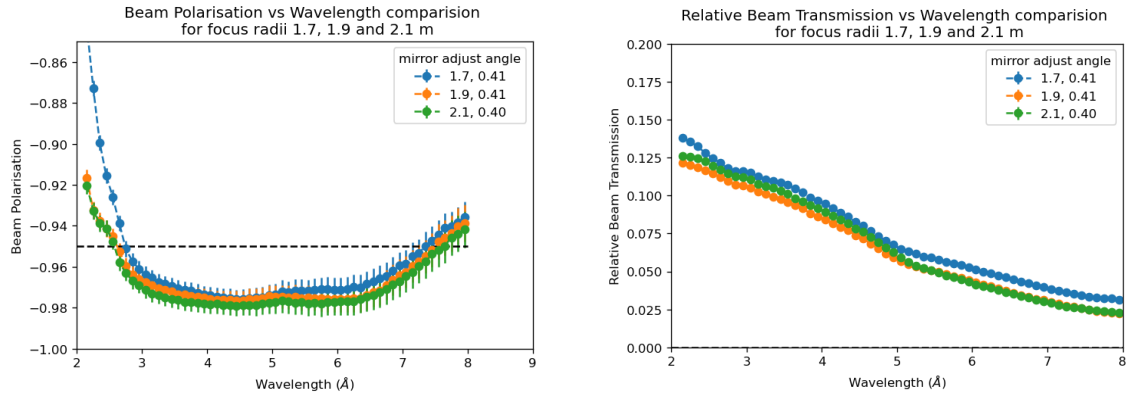

Fig. 34: Performance vs Focus; Mirror adjust angle (a) Comparison of beam polarisation vs wavelength (b) Comparison of relative beam transmission vs wavelength.

Using the parameters that give the best performance (**Focus 2.1 m and adjust angle 0.4°**), we obtain the polarisation and intensity cross-sectional profile at the pinhole and at 5 m distance from the pinhole using wavelength detectors and position-sensitive detectors (fig. 35).

Fig. 35 (a) shows the polarisation cross-sectional at the pinhole. Here, it can be seen that the beam is polarised in spin down state and these are transmitted neutrons. While the spin-up neutrons get reflected out of the beam and are absorbed by the channel walls.

Fig. 35 (b) shows the intensity cross-sectional at the pinhole. The intensity profile appears to be quite homogeneous. There is slight variation which is consistent with the variation observed in simulations without the v-cavity. The effects of the channel dividers are slightly visible.

The polarisation and intensity profiles at 5 m distance from pinhole are shown in fig 35 (c) and (d), respectively. Fig. 35 (c) shows that the polarisation is good enough (which is the primary requirement) in the area of interest which is 5 x 5 cm field of view. Field of view for typical analysers mostly Solid-State Benders is 5 x 5 cm and even if Helium-3 analyser is used, the field of view is still with 10 x 10 cm. In figure 35 (c) and (d), maximum field of view is 10 x 10 cm, while essential field of view is 5 x 5 cm, and the polarisation and transmission in this field of view fulfils the requirements mentioned as goals.

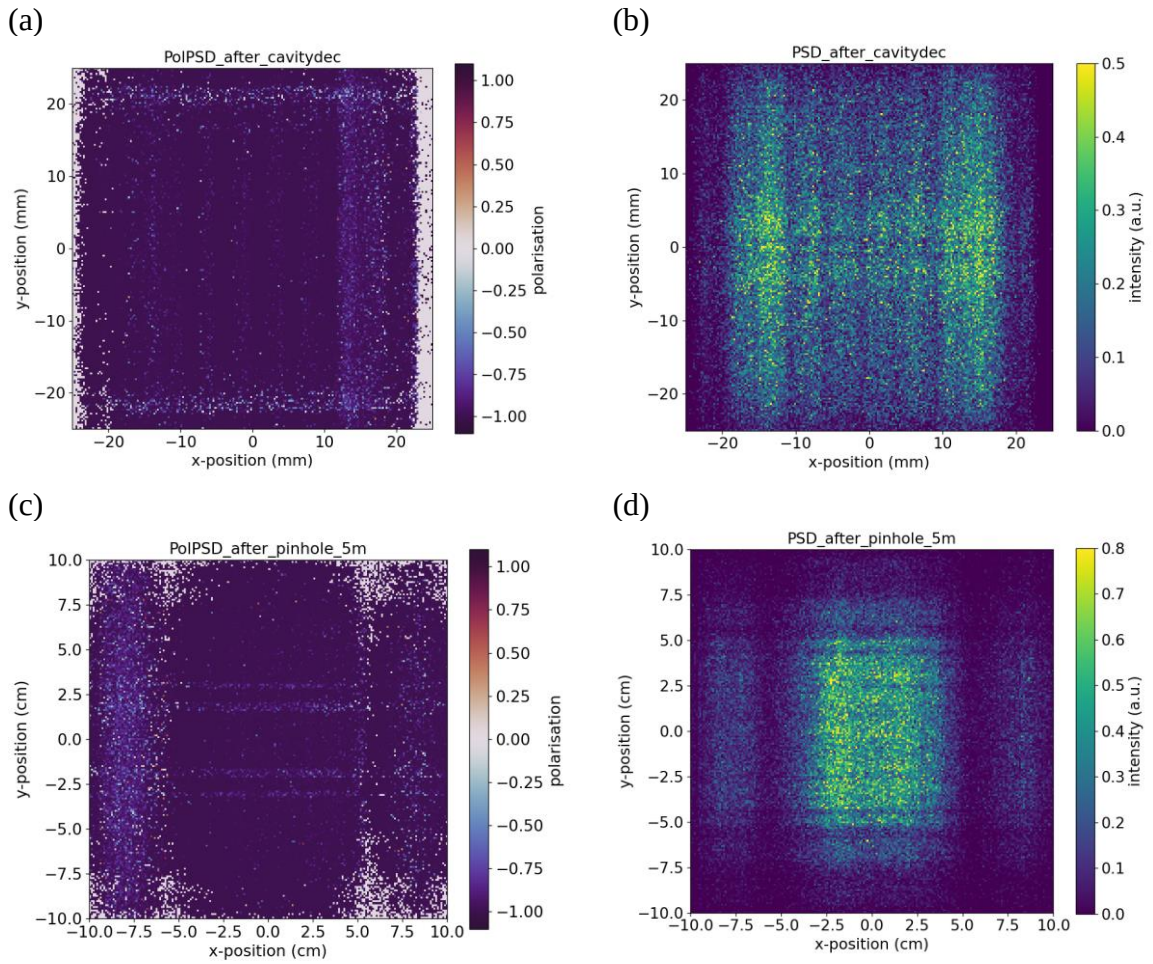

Fig. 35: Cross-sectional profiles after the cavity (a) polarisation at detector (3 x 3 cm) at pinhole, (b) intensity at detector (3 x 3 cm) at pinhole, (c) polarisation at detector (20 x 20 cm) at 5 m distance from pinhole, (d) intensity at detector (20 x 20 cm) at 5 m distance from pinhole. The v-cavity polariser has a focus radius = 2.1 m and mirror adjust angle = 0.4°

5. Magnetic field environment for polariser

At the minimum, an experimental setup consists of a polariser, spin-flippers, guide fields, a sample, an analyser and a detector. Magnetic fields are imposed along the neutron flight path from the polariser to the analyser. The magnetic field maintains the neutron polarisation and is also required for the performance of the polariser and analyser. The requirements for the magnetic field of the polariser are:

1) It should be strong enough to saturate the magnetisation of the polarising supermirror. The field strength must be > 30mT;
2) It should be homogeneous with the angle between the field direction and mirror surface be < 5°.

In only a few cases there can be analytic solution of the magnetic field generated by permanent magnets and coils. In practice, computation methods such as finite element method are used to solve the Maxwell's equations to calculate the magnetic field given the field components.

5.1 Finite element method

Finite element method (FEM) is used for solving partial differential equations such as the Maxwell's equations to analyse the behaviour of physical systems [19]. To solve a given problem, the FEM subdivides a large system into smaller, simpler parts called finite elements. This is achieved by a discretization of a continuous domain by the creating a mesh. The physics in a small element can then be represented by linear algebraic equations which contains the physics of the element itself and its connection to the surrounding elements. The simple equations that model these finite elements are then assembled into a larger system of linear equations. To solve this system of linear equation, FEM uses an error function that estimates the error between the numerical solution and the true solution. It then approximates a solution by minimizing the error. For this work, we use COMSOL Multiphysics® [20] which is a FEM software package that can calculation the magnetic fields from an input of the field elements. Within this it is possible to design and optimize the magnetic field environment provided by the magnetic housing for the polariser.

5.2 Magnetic Housing for polariser

The magnetic housing for the polariser consists of permanent magnets and steel plate as shown in fig. 36. In the figure, the polariser region is represented by a rectangle 70 cm long × 3 cm wide × 4.5 cm tall. Two arrays of six uniformly spaced magnets provides the magnetic field source. The magnets are grade N52 NdFeB magnets (remanent magnetisation 1.44 T) with 5 cm × 2 cm cross-section and 14.5 cm tall. They are magnetised with the north-pole pointing down. The magnetic flux feeds into steel plates above and below the polariser. The 70 cm long × 20 cm wide × 5 mm thick steel plates are made of s235 tool steel. Magnetic field emits from the inner surfaces of the plates with the magnetic north pointing upward.

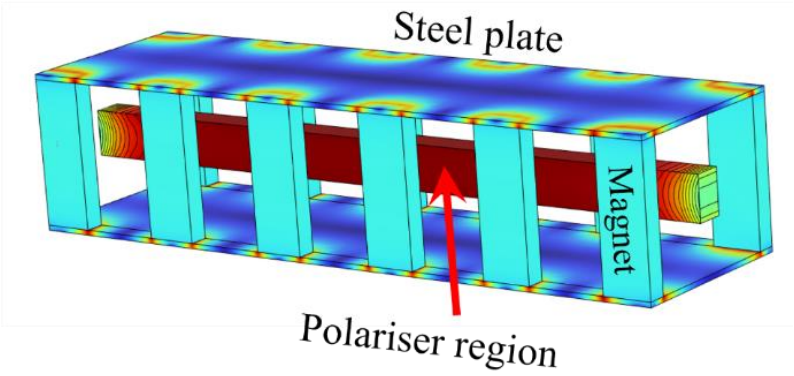

Fig. 36: Magnetic housing for polariser and the polariser region

5.3 Results of field calculation

The magnetic field strength map over the polariser region is shown in fig. 37 (a). The centre of the polariser region has close to 55 mT field. Near the two ends of the region along the length, the field strength decreases. The field strength is the weakest at the centre of the end faces. We plot the field strength map on the central horizontal plane (fig. 37 (b)) and central vertical plane (fig. 37 (c)) to determine what the lowest field strength is and found it to be close to 42 mT. As the minimum field strength required to saturate the polarising supermirrors is 30 mT. The magnetic housing will provide sufficient field strength for the polariser.

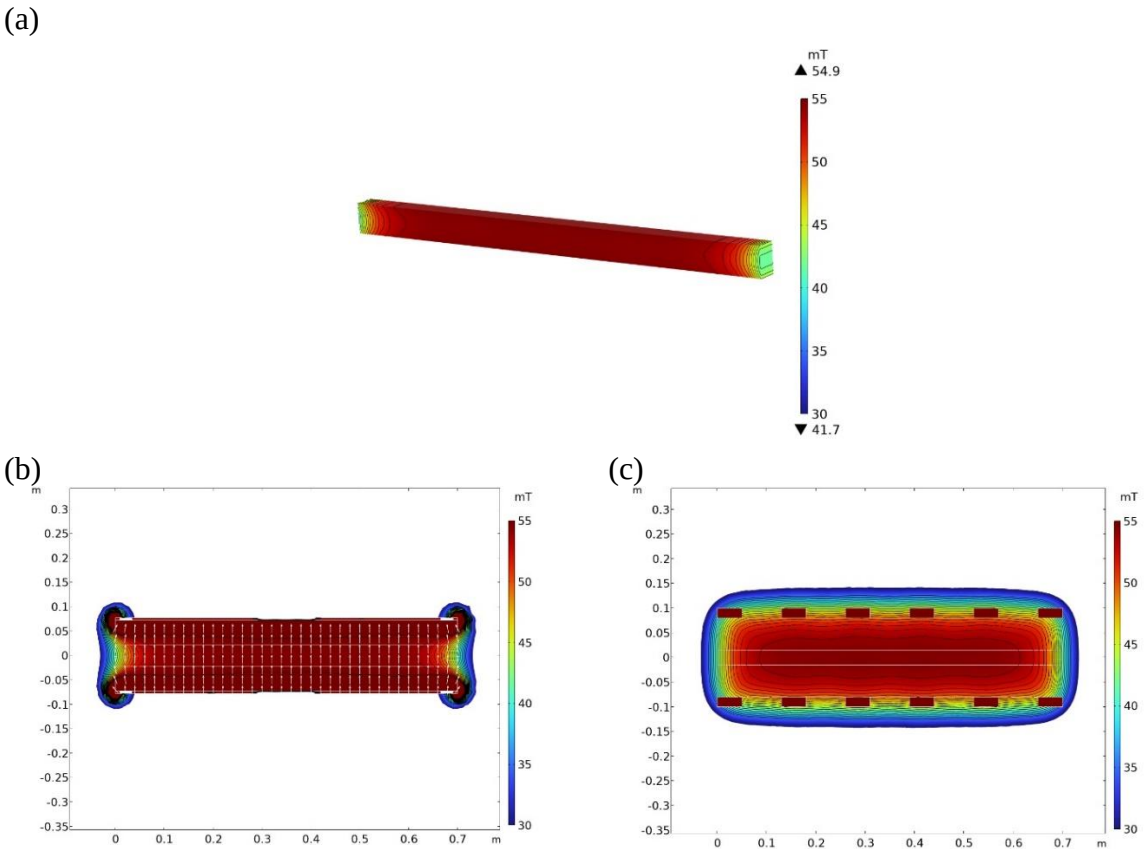

Fig. 37: Magnetic field strength in polariser region: (a) overview, (b) on vertical central plane, (c) on horizontal central plane

The angle between the magnetic field and the supermirror surface should be kept to a minimum. At a given angle θ, when a perfectly polarised beam with its polarisation vector parallel to the magnetic field impinges on the supermirror surface, the polarisation of the beam as seen by the supermirror becomes cos θ. At 5°, the beam polarisation would be reduced from 100% to 99.6%. This is the maximum acceptable loss. The field angle over the polariser region is plotted in fig. 38 (a). The field angle is large at the vertical edge of the region. Fig. 38 (b) shows the field angle plot at that location. The field angles that deviate most from the supermirror surface are determined to be ±0.24° which is well below the limit. The magnetic housing will provide a field with sufficient alignment to the supermirrors.

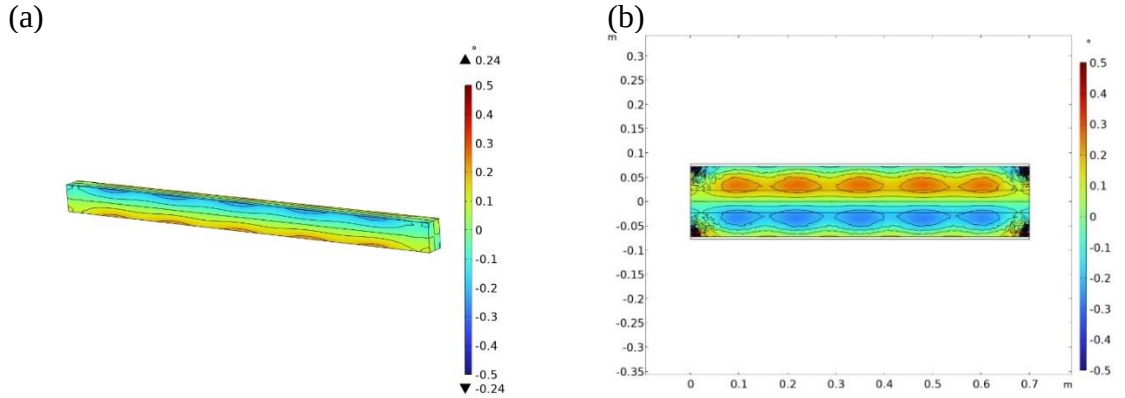

Fig. 38: Magnetic field angle in polariser region: (a) overview, (b) on vertical plane at the edge of the region where the field angle would be the largest

6. Summary

In this work, the principles of polarised neutron were introduced and an example of using polarised neutron imaging was given, where magnetic domains and domain walls were studied. Further, different types of polarisers were described and the selection of a v-cavity polariser was established to produce a polarised neutron beam on the ODIN imaging instrument at the ESS.

The main part of this work is a design study of this polarizer, with the aim to match the beam characteristics of ODIN. Using Monte Carlo ray-tracing simulations to evaluate the device performance, the key parameters were determined that will produce a polarised neutron beam with at least 95% polarisation over ODIN's wavelength range, from 2.5 Å to 7.5 Å, and that will have an acceptable transmission and cross-sectional intensity profile. Additionally, the design of a magnetic housing was evaluated using finite element method to compute the magnetic field. The design was found to fulfill the magnetic field requirements of the polariser.

In conclusion, a polariser design, including a magnetic housing, was designed, which is suitable to be used at the ODIN instrument at ESS, according to the specified requirements.

ACKNOWLEDGEMENT

First of all, I want to express my sincere appreciation to Prof. Dmytro Orlov for his continuous support throughout my Master's programme, including inviting me to be a part of his Materials Team and facilitating connection with scientists at the European Spallation Source (ESS) for my master's thesis work. His advice has been most helpful to me.

I also extend my gratitude to my thesis supervisors Dr. Wai Tung Lee, Senior Scientist for Polarisation at ESS and Dr. Alex Backs, Postdoctoral fellow at Lund University for their continuous guidance, patience, encouragement and for sharing immense knowledge during my thesis research.

Additionally, I thank Dr. Manuel Morgano, Instrument Scientist for ODIN, ESS for his assistance with the information about ODIN instrument and addressing my queries.

Special thanks go to Dr. Peter Kjær Willendrup, Senior Research Engineer at Technical University of Denmark, DTU and Dr. Mads Bertelsen, Computational Neutron Scattering Scientist at ESS for introducing me to McStas Monte-Carlo ray tracing and involving me in the McStas training programme.

The completion of my thesis work could not have been achieved without the support of all these mentors and my parents, who have supported me in every aspect of my life.

APPENDIX

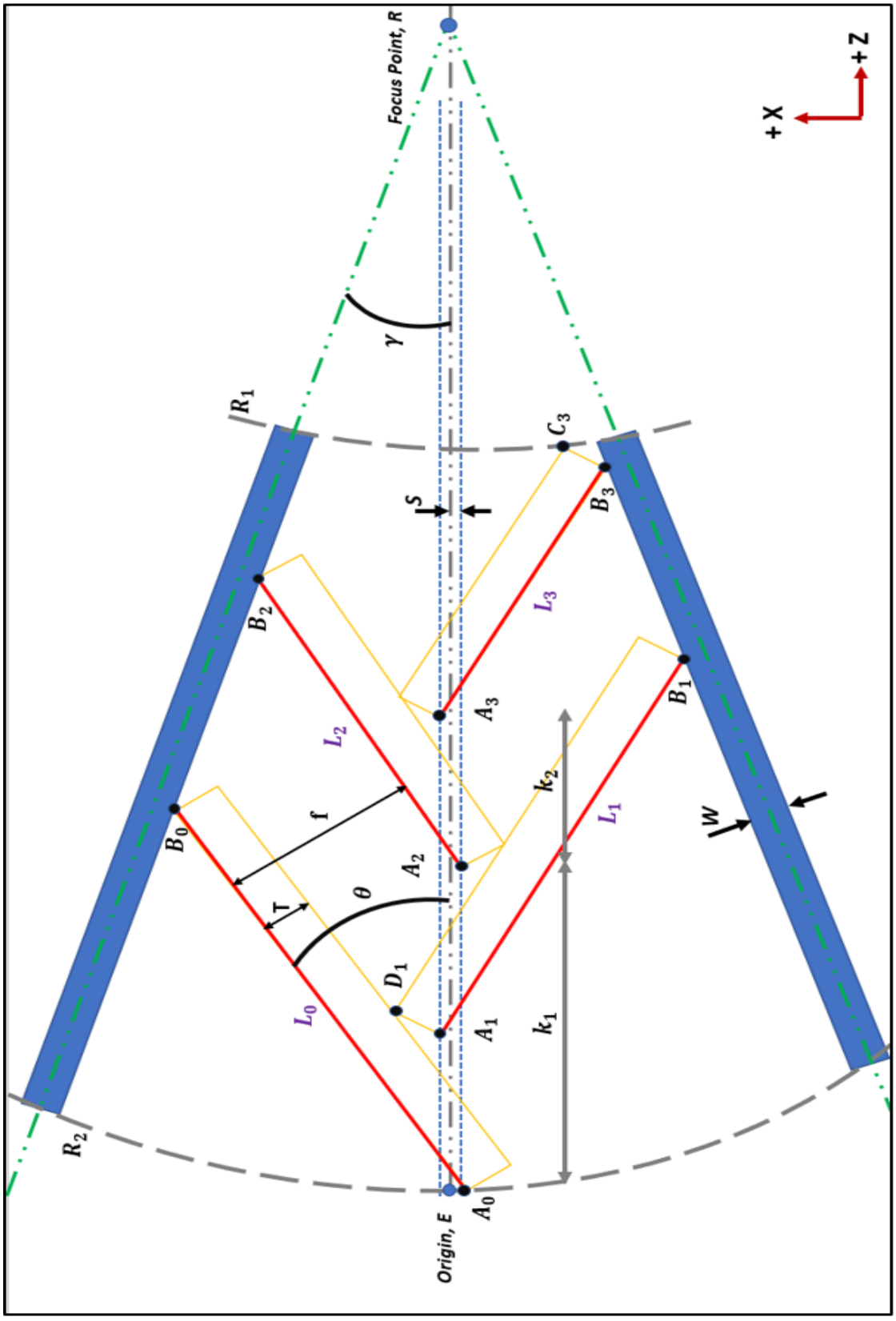

Fig 39: Schematic of the single channel of the focused v-cavity

1) Finding the positions of the points A_0, A_1, A_2 and A_3 through k_1 and k_2

a) **b)**

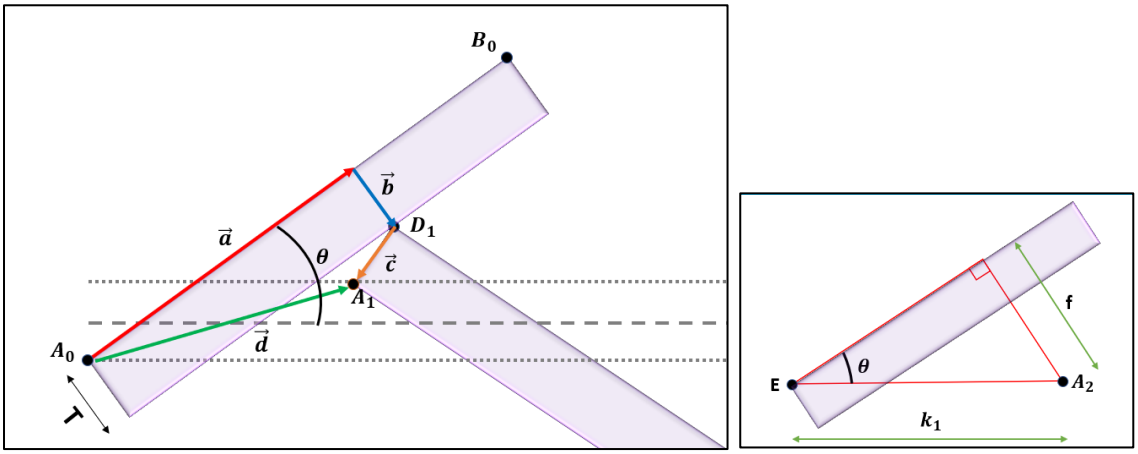

Fig 40: Geometry of mirrors including the vectors used in the derivations, for a) mirrors touching each other at corner D_1, and b) the minimum distance between two mirrors, k_1

The mirrors need to be placed as closely as possible which is constrained by them touching each other at the corner D_i. The separation along the z-axis between two mirror positions, k_2 can be found from the equation.

Using Vector addition, from figure 40 (a), we get-

$$\vec{d} = \vec{a} + \vec{b} + \vec{c} \tag{1}$$

With the vectors as defined in figure 40 (a),

$$\vec{a} \equiv (x, y, z) \equiv \lambda sin\,\theta\ , 0\ , \lambda\, cos\,\theta \quad (i)$$
$$\vec{b} \equiv (x, y, z) \equiv -T\, cos\,\theta\ , 0\ ,\ T sin\,\theta \quad (ii)$$
$$\vec{c} \equiv (x, y, z) \equiv -T\, cos\,\theta\ , 0\ , -T sin\,\theta \quad (iii)$$
$$\vec{d} \equiv (x, y, z) \equiv 2S\ , 0\ , k_2 \quad (iv)$$

Separating the x- and z-component, we get-

For X-component, $2S = \lambda sin\,\theta\ - T\, cos\,\theta - T\, cos\,\theta$

$$\therefore\ \lambda = \frac{2S + 2T\, cos\,\theta}{sin\,\theta} \tag{2}$$

For Z-component, $k_2 = \lambda\, cos\,\theta + T sin\,\theta\ - T sin\,\theta$

$$\therefore\ k_2 = \lambda\, cos\,\theta \tag{3}$$

The second constraint for the mirror placement is the minimum distance between parallel mirrors, f . From this we obtain a second separation along the z-axis, k_1 , for mirror 0 & mirror 2 and mirror 1 & mirror 3.

From figure 40 (b), we get-

$$\sin\theta = \frac{f}{k_1}$$

$$\therefore \quad \boldsymbol{k_1 = \frac{f}{\sin\theta}} \tag{4}$$

The z-positions of mirrors 0 and 1 are always at 0 and k_2, respectively. For mirror 2, we need to check if $2k_2$ or k_1 has the larger value, which then will be used for the placement of the mirrors alongside fulfilling both the constraints mentioned above. Mirror 3 is then placed at k_2 behind mirror 2.

2) Finding the expression for length of supermirror, L_3

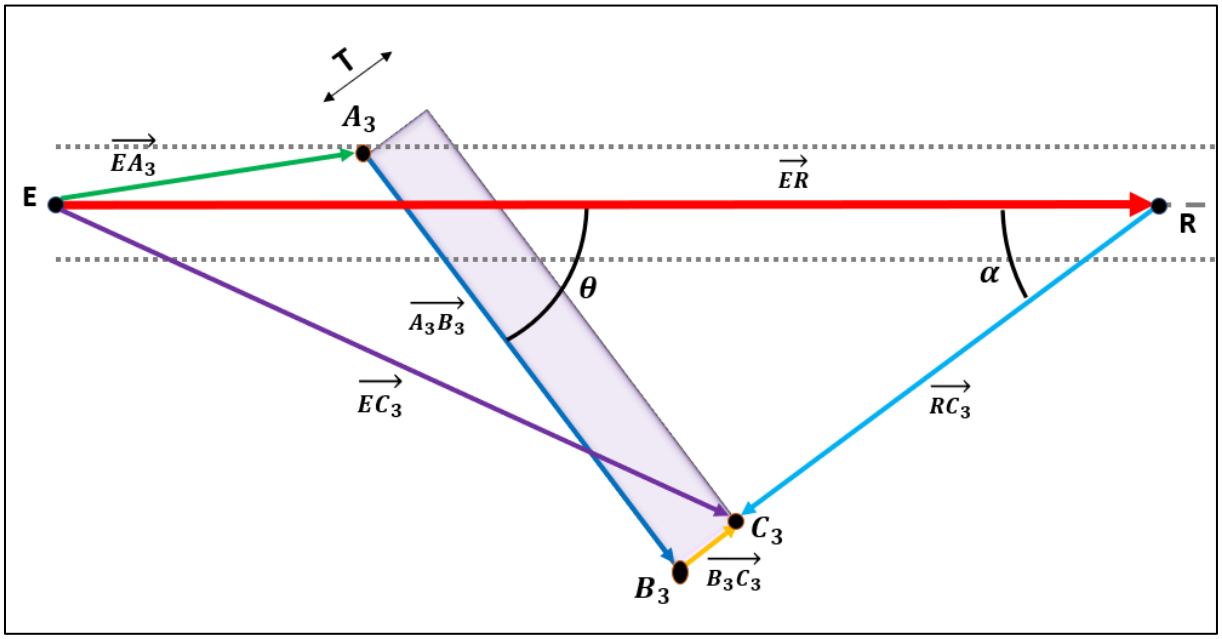

Fig 41: Geometry of mirror including the vectors used in the derivations for mirror corner C_3 touching R_1

From the task 1, now we have the positions of points A_0, A_1, A_2 and A_3, but this last mirror with length L_3 should not go outside the device i.e., R_1, which implies that the point C_3 should be touching R_1. So, we need to solve for this constraint.

Using Vector addition, from figure 41, we get-

$$\boldsymbol{\overrightarrow{EC_3} = \overrightarrow{EA_3} + \overrightarrow{A_3B_3} + \overrightarrow{B_3C_3} = \overrightarrow{ER} + \overrightarrow{RC_3}} \tag{5}$$

With the vectors as defined in figure 41,

$\boldsymbol{\overrightarrow{A_3B_3} \equiv (x,y,z) \equiv -L_3 \sin\theta\ , 0\ ,\ L_3 \cos\theta}$ *(i)*
$\boldsymbol{\overrightarrow{B_3C_3} \equiv (x,y,z) \equiv T\cos\theta\ , 0\ ,\ T\sin\theta}$ *(ii)*
$\boldsymbol{\overrightarrow{EA_3} \equiv (x,y,z) \equiv S\ , 0\ , A_{3z}}$ *(iii)*
where, $A_{3z} = k_1 + k_2$ or $3k_2$
$\boldsymbol{\overrightarrow{RC_3} \equiv (x,y,z) \equiv -R_1 \sin\alpha\ , 0\ , -R_1 \cos\alpha}$ *(iv)*
$\boldsymbol{\overrightarrow{ER} \equiv (x,y,z) \equiv 0\ , 0\ , R_2}$ *(v)*

Separating the x- and z-component for equations *i*, *ii* and *iii*, we get-

For X-component, $EC_{3_x} = S - L_3 \sin\theta + T\cos\theta$ **(*vi*)**

For Z-component, $EC_{3_z} = A_{3z} + L_3\cos\theta + T\sin\theta$ (*vii*)

Separating the x- and z-component for equations *iv* and *v*, we get-

For X-component, $EC_{3_x} = -R_1 \sin\alpha$ (*viii*)

For Z-component, $EC_{3_z} = R_2 - R_1\cos\alpha$ (*ix*)

Equating EC_{3_x} from equations *vi* and *viii*, we get-

$S - L_3 \sin\theta + T\cos\theta = -R_1 \sin\alpha$

$$\therefore \boldsymbol{L_3 = \frac{S + T\cos\theta + R_1 \sin\alpha}{\sin\theta}} \quad \textbf{(6)}$$

Equating EC_{3_z} from equations *vii* and *ix*, we get-

$EA_{3_z} + L_3\cos\theta + T\sin\theta = R_2 - R_1\cos\alpha$

$$\therefore \boldsymbol{L_3 = \frac{R_2 - R_1\cos\alpha - EA_{3_z} - T\sin\theta}{\cos\theta}} \quad \textbf{(7)}$$

So, solving for α using equations 7 and 8, we get-

$$\frac{S + T\cos\theta + R_1\sin\alpha}{\sin\theta} = \frac{R_2 - R_1\cos\alpha - EA_{3_z} - T\sin\theta}{\cos\theta}$$

$$\therefore \boldsymbol{\alpha = \sin^{-1}\left(\frac{R_2\sin\theta - EA_{3_z}\cdot\sin\theta - T - S\cos\theta}{R_1}\right) - \theta} \quad (8)$$

3) Solving for half of the opening angle of channel, γ

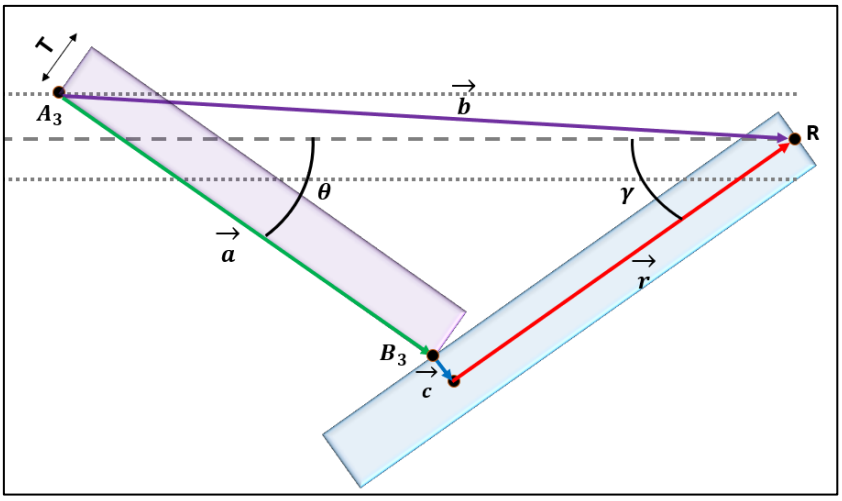

Fig 42: Geometry of mirrors including the vectors used in the derivations for mirror corner B_3 touching the divider

Once the constraint with regards to point C_3 is resolved, it can be understood that point B_3 is touching the divider. So, we need to solve for this constraint and through this its easier approach to find the expression for γ.

Using Vector analysis, from figure 42, we get-

$$\vec{r} = \vec{b} - \vec{a} - \vec{c} \tag{9}$$

With the vectors as defined in figure 42,

$\vec{a} \equiv (x, y, z) \equiv -L_3 sin\,\theta\ , 0\ , L_3 cos\,\theta$ *(i)*
$\vec{b} \equiv (x, y, z) \equiv -S, 0\ , R_2 - A_{3_Z}$ *(ii)*
$\vec{c} \equiv (x, y, z) \equiv -0.5W\,cos\,\gamma\ , 0\ , 0.5W sin\,\gamma$ *(iii)*
$\vec{r} \equiv (x, y, z) \equiv \delta \sin\gamma\ , 0\ , \delta \cos\gamma$ *(iv)*

Separating the x- and z-component for equations, we get-

For X-component, $\delta \sin\gamma = -S + L_3 sin\,\theta + 0.5W\,cos\,\gamma$

$$\therefore\ \delta = \frac{-S + L_3 sin\,\theta + 0.5W\,cos\,\gamma}{sin\,\gamma} \tag{10}$$

For Z-component, $\delta \cos\gamma = R_2 - A_{3_Z} - L_3 cos\,\theta - 0.5W sin\,\gamma$

Solving for γ using both the equations, we get –
$(-S + L_3 sin\,\theta + 0.5W\,cos\,\gamma)\,.\cos\gamma = (R_2 - A_{3_Z} - L_3 cos\,\theta - 0.5W sin\,\gamma)\,.\sin\gamma$

Let, $R_2 - A_{3_Z} - L_3 cos\,\theta = A$ and $L_3 sin\,\theta - S = B$, we get –
$\therefore A \sin\gamma = B\,cos\,\gamma + 0.5W$
$\therefore A \sin\gamma - 0.5W = B(\sqrt{1 - \sin^2\gamma}\ )$

Squaring both sides, we get-
$\therefore (A \sin\gamma - 0.5W)^2 = (B)^2.(1 - \sin^2\gamma)$
$\therefore (A^2 + B^2).\sin^2\gamma + (-W.A).\sin\gamma + (0.5^2.W^2 - B^2) = 0$
With, $A^2 + B^2 = K$, $-W.A = L$ and $0.5^2.W^2 - B^2 = M$,

$$\sin\gamma = \frac{-L \pm \sqrt{L^2 - 4KM}}{2K}$$

Considering only single root i.e., only one solution for γ as this angle influences the spin states of neutrons as they interact with the polariser. The enhancement of reflectivity of neutrons with specific spin states is achieved by precisely controlling γ.

So, $\gamma = \sin^{-1}\left(\frac{-L - \sqrt{L^2 - 4KM}}{2K}\right)$ (11)

4) Generalized expression for all the lengths of supermirror

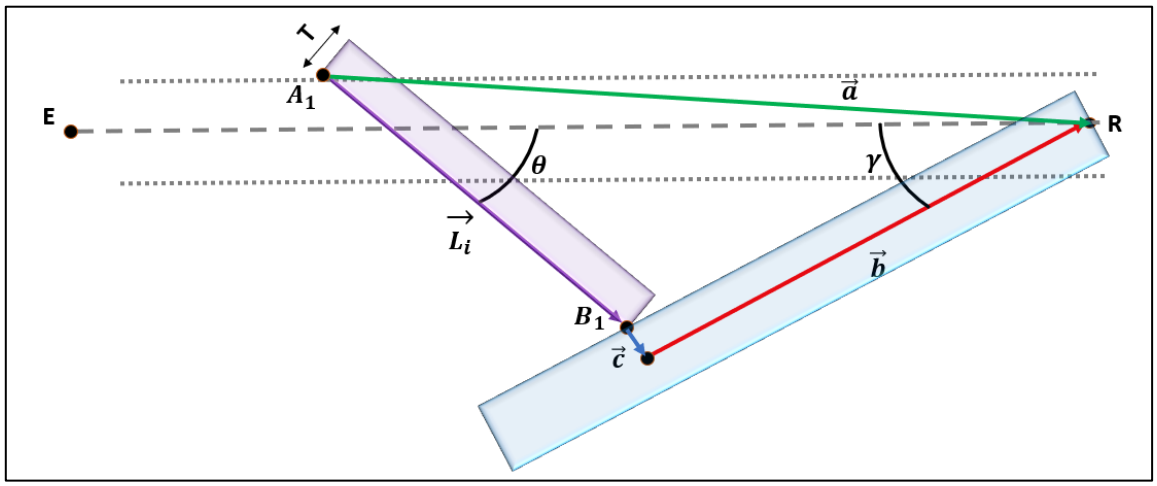

Fig 43: Geometry of mirrors including the vectors used in the derivations for calculation of length of supermirrors, L_i

Since we have derived the expression for γ, it is now possible to calculate lengths of all the supermirrors. For calculations to be easy, finding the general expression for length by solving for L_1.

Using Vector analysis, from figure 43, we get-

$$\vec{b} = \vec{a} - \vec{L_1} - \vec{c} \tag{12}$$

With the vectors as defined in figure 43,

$$\vec{L_1} \equiv (x, y, z) \equiv -L_1 sin\,\theta\ , 0\ , L_1 cos\,\theta \quad (i)$$
$$\vec{a} \equiv (x, y, z) \equiv -S, 0\ , R_2 - A_{1_z} \quad (ii)$$
$$\vec{c} \equiv (x, y, z) \equiv -0.5W\,cos\,\gamma\ , 0\ , 0.5W sin\,\gamma \quad (iii)$$
$$\vec{b} \equiv (x, y, z) \equiv \phi \sin\gamma\ , 0\ , \phi \cos\gamma \quad (iv)$$

Separating the x- and z-component for equations, we get-

For X-component, $\phi \sin\gamma = -S + L_1 sin\,\theta + 0.5W\,cos\,\gamma$

$$\therefore\ \phi = \frac{-S + L_1 sin\,\theta + 0.5W\,cos\,\gamma}{sin\,\gamma} \tag{13}$$

For Z-component, $\phi \cos\gamma = (R_2 - A_{1_z}) - L_1 cos\,\theta - 0.5W sin\,\gamma$

Solving for L_1 using both the equations, we get –

$(-S + L_1 sin\,\theta + 0.5W\,cos\,\gamma)\,.\cos\gamma = (R_2 - A_{1_z} - L_1 cos\,\theta - 0.5W sin\,\gamma)\,.\sin\gamma$

Rearrange the terms, the generic expression for length of supermirrors, L_i can be written as,

$$L_i = \frac{S.\cos\gamma + (R_2 - A_{i_z}).\sin\gamma - 0.5W}{\sin(\gamma + \theta)}$$

With the relevant changes in term A_{i_z} in the entire expression, we can calculate the lengths of all supermirrors.

REFERENCES

[1] N. Kardjilov, I. Manke, A. Hilger , M. Strobl and J. Banhart , "Neutron Imaging in Materials Science," *Materials Today,* vol. 14, no. 6, p. 248, 2011.

[2] M. Strob, H. Heimonen, S. Schmidt, M. Sales, N. Kardjilov, A. Hilger, I. Manke, T. Shinohara and J. Valsecchi, "Topical review: Polarisation measurements in neutron imaging," *Journal of Physics D: Applied Physics,* vol. 25, p. 123001, 2019.

[3] Andersen K. H., et. al., "The instrument suite of the European Spallation Source," *Nuclear Instruments & Methods in Physics Research Section a-Accelerators Spectrometers Detectors and Associated Equipment,* vol. 957, no. 39, p. 163402, 2020.

[4] M. Strobl, "The Scope of the Imaging Instrument Project ODIN at ESS," *Physics Procedia,* vol. 69, pp. 18-26, 2015.

[5] A. Backs, S. Sebold, M. Busi, W. T. Lee, M. Strobl and D. Orlov, "Development and first results of a magnetic sample environment for polarized neutron imaging of thin metal sheets," *EPJ Web of Conferences,* vol. 286, no. 05003.

[6] G. Russell, "Spallation physics - an overview," *Proceedings of ICANS-XI Internationl collaboration on advanced neutron sources, KEK, Tsukuba,* p. 25, 1990.

[7] T. R. Gentile, E. Babcock, J. A. Borchers, W. C. Chen, D. Hussey, G. L. Jones, W. T. Lee, C. F. Majkrzrok, K. V. O'Donovon, W. M. Snow, X. Tong, S. G. E. te Velthuis, T. G. Walker and H. Yan, "Polarized 3He spin filters in neutron scattering," *Physica B: Condensed Matter,* vol. 356, no. 1-4, pp. 96-102, 2005.

[8] M. Batz, P. Nacher and G. Tastevin, "Fundamentals of metastability exchange optical pumping in helium," *J. Phys.: Conf. Ser,* vol. 294, p. 0120002, 2011.

[9] P. Courtois, B. Hamelin and K. H. Andersen, "Production of copper and Heusler alloy Cu2MnAl mosaic single crystals for neutron monochromators," *Nuclear Instruments and Methods in Physics Research Section A: Accelerators, Spectrometers, Detectors and Associated Equipment,* vol. 529, no. 1-3, pp. 157-161, 2004.

[10] F. Mezei, "Very High Reflectivity Supermirrors And Their Applications," *Proc. SPIE 0983: Thin Film Neutron Optical Devices: Mirrors, Supermirrors, Multilayer Monochromators, Polarizers, and Beam Guides,* 1989.

[11] T. Krist and F. Mezei, "Solid state neutron polarizers and collimators," *Proc. SPIE 4509, Neutron Optics,* 2001.

[12] Neutron data booklet 2nd edition, 2 ed., Institute Laue Langevin: Old City Publishing Group, ISBN: 0-9704143-7-4, 2003.

[13] H. Kiessig, "Untersuchungen zur totalreflexion von röntgenstrahlen," *Annalen der Physik,* vol. 402.6, pp. 715-768, 1931.

[14] H. Kiessig, "Interferenz von Röntgenstrahlen an dünnen Schichten," *Ann. Phys.,* vol. 402, pp. 769-788, 1931.

[15] S. J. Callori, C. Rehm, G. L. Causer, M. Kostylev and F. Klose, "Hydrogen Absorption in Metal Thin Films and Heterostructures Investigated in Situ with Neutron and X-ray Scattering," *Metals,* vol. 6, no. 6, p. 125, 2016.

[16] C. Schanzer, M. Schneider and P. Böni, "Neutron Optics: Towards Applications for Hot Neutrons," *Journal of Physics Conference Series,* vol. 746, no. 1, p. 012024, 2016.

[17] P. Willendrup and K. Lefmann, "McStas (i): Introduction, use, and basic principles for ray-tracing simulations," *J. Neutron Res.,* vol. 22, pp. 1-16, 2020.

[18] P. Willendrup and K. Lefmann, “McStas (ii): An overview of components, their use, and advice for user contributions,” *Journal of Neutron Research,* vol. 23, pp. 7-27, 2021.

[19] J. M. Jin, The finite element method in electromagnetics, John Wiley & Sons,, 2015, pp. 170-181.

[20] COMSOL Multiphysics®, www.comsol.com. COMSOL AB, Stockholm, Sweden.